

1 **Mechanistic investigations of the formation of multifunctional**
2 **products from the multi-generation OH oxidation of styrene**

3 Long Chen,^{1,2,3} Yu Huang,^{*,1,2,3} Yonggang Xue,^{1,2,3} Long Cui,^{1,2,3} Zhihui Jia⁴

4 ¹ *State Key Laboratory of Loess Science, Institute of Earth Environment, Chinese*
5 *Academy of Sciences, Xi'an 710061, China*

6 ² *National Observation and Research Station of Regional Ecological Environment*
7 *Change and Comprehensive Management in the Guanzhong Plain, Xi'an 710061,*
8 *China*

9 ³ *Shaanxi Key Laboratory of Atmospheric and Haze-fog Pollution Prevention, Xi'an*
10 *710061, China*

11 ⁴ *School of Materials Science and Engineering, Shaanxi Normal University, Xi'an,*
12 *Shaanxi, 710119, China*

13

14

15

16

17 Submitted to *Atmospheric Chemistry & Physics*

18

19

20

21 *Corresponding author:

22 Prof. Yu Huang, E-mail address: huangyu@ieecas.cn

23

24 **Abstract**

25 Styrene is a highly reactive aromatic hydrocarbon that has been identified as a
26 key secondary organic aerosol (SOA) precursor. Recent laboratory chamber
27 experiments have identified C₇ and C₈ series compounds as the main components of
28 SOA in the photooxidation of styrene. However, their molecular structures and
29 formation pathways remain largely uncharacterized. Herein, the formation
30 mechanisms of multifunctional products from the multi-generation OH oxidation of
31 styrene are studied using the quantum chemistry methods. The calculations show that
32 the first generation RO₂ radicals can either proceed unimolecular decomposition to
33 yield benzaldehyde (C₇H₆O), or undergo bimolecular reactions with HO₂/NO to form
34 the first generation closed-shell C₇- and C₈-products, hydroperoxide 1st-ROOH
35 (C₈H₁₀O₃), benzaldehyde, and organic nitrate 1st-RONO₂ (C₈H₉NO₃). For the second
36 generation OH oxidation, OH-addition reaction occurring at the *ortho*-site of
37 1st-ROOH and 1st-RONO₂ has a significant dominance. The *ortho*-OH-addition
38 products can proceed through two O₂-addition steps and a cyclization process to
39 produce the peroxide bicyclic peroxy radicals (BPR). BPR can further react with
40 HO₂/NO to form the second generation closed-shell C₈-products, hydroperoxide
41 2nd-ROOH (C₈H₁₂O₈), organic nitrate 2nd-RONO₂ (C₈H₁₀N₂O₁₀), and other
42 multifunctional products, in which the first two products have fractional yields of 41.4%
43 and 4.8%, respectively. For the third generation OH oxidation, OH-addition
44 occurring at the C=C double bond of 2nd-ROOH and 2nd-RONO₂ has the lowest
45 barrier. The major third generation closed-shell C₈-products are the multifunctional
46 hydroperoxides and organic nitrates. These findings carry important implications for
47 advancing our understanding of the chemical composition and formation mechanisms
48 of aromatic SOA.

49

50 **1. Introduction**

51 Aromatic compounds are recognized as the significant secondary organic aerosol
52 (SOA) precursors, accounting for 20%-30% of the total volatile organic compounds

53 (VOCs) and up to ~60% of the urban atmosphere (Xu et al., 2020; Yan et al., 2019; Yu
54 et al., 2022; Cabrera-Perez et al., 2016; Iyer et al., 2023; Wang et al., 2017; Bloss et
55 al., 2005; Forstner et al., 1997). The primary sources include the incomplete
56 combustion, solvent evaporation, and industrial emission, and the secondary sources
57 involve the biofuel and biomass burning (Xu et al., 2020; Cabrera-Perez et al., 2016;
58 Li et al., 2019). The most abundant aromatic compounds, including benzene, toluene,
59 ethylbenzene, xylenes, styrene and trimethylbenzenes, are highly present in urban
60 environments (Cabrera-Perez et al., 2016; Koppmann, 2008). The degradation of
61 aromatic compounds initiated by the atmospheric oxidants (e.g., OH radicals, NO₃
62 radicals, O₃, and Cl atom) leads to the production of multifunctional molecules (e.g.,
63 nitroaromatics, dicarbonyls, cresols, epoxides) (Ji et al., 2017; Wu et al., 2014; Fu et
64 al., 2023; Wang and Li, 2021; Wang et al., 2013; Zaytsev et al., 2019; Wang et al.,
65 2020), significantly contributing to new particle formation (NPF) and SOA formation
66 (up to 50% in eastern China) in the atmosphere (Wang et al., 2017; Wang et al., 2020;
67 Garmash et al., 2020; Molteni et al., 2018; Nie et al., 2022).

68 The secondary organic aerosol formation potential (SOAP) of aromatics is
69 significantly greater than that of alkanes and alkenes during haze episodes in Beijing
70 (Sun et al., 2016). Among these precursors, toluene is the predominant SOA-forming
71 species, contributing more than 16% of the total SOA, followed by styrene (15%) and
72 ethylbenzene (9.5%) (Sun et al., 2016). Styrene is primarily emitted from the
73 anthropogenic activities such as solvent usage and vehicle exhaust (Cho et al., 2014;
74 Wu et al., 2021), which is detected at the ppb levels in urban environments, with the
75 mixing ratios of 0.06-4.50 ppb (Cho et al., 2014; Huang et al., 2019). Styrene has
76 been classified as a hazardous air pollutant in the 1990 Clean Air Act due to the
77 potential mutagen and carcinogen (Environmental Protection Agency (EPA), 1990).
78 Therefore, it is very necessary to investigate the degradation mechanisms of styrene
79 under atmospheric conditions. In general, the atmospheric oxidation of styrene
80 initiated by OH radicals is anticipated to be the dominant daytime sink, and the
81 lifetime is estimated to be ~ 8 h under the conditions of typical OH radicals
82 concentrations ($[OH] = \sim 2 \times 10^6 \text{ molecules cm}^{-3}$) (Wu et al., 2021; Shen et al., 2022).

83 Due to the existence of highly reactive vinyl and aromatic groups, OH-initiated
84 oxidation of styrene mainly comprise two kinds of pathways: H-abstraction and
85 OH-addition, in which C_β-site OH-addition reaction is expected to be the predominant
86 pathway (Wu et al., 2021; Wang et al., 2015; Zhang et al., 2024). The formed products
87 can combine with an O₂ molecule leading to the first generation peroxy radicals,
88 which can further react with NO resulting in the formation of benzaldehyde and
89 formaldehyde. The barrier of the rate-limiting step is predicted to be 28.4 kcal/mol
90 (Wang et al., 2015), implying that benzaldehyde is unlikely to be the sole primary
91 product in the oxidation of styrene due to their higher barriers. Additionally, carbonyl
92 oxides, formed in the ozonolysis of styrene, serve as the chain units participating in
93 the formation of oligomers (Yu et al., 2022). The volatility of oligomers decreases
94 dramatically as the successive addition of carbonyl oxides increases, eventually
95 transforming into extremely low volatility organic compounds (ELVOC) and directly
96 participating in NPF.

97 Experimentally, Cho et al., investigated the kinetics of the reaction styrene
98 + OH at 240-340 K and 1-3 Torr using the mass spectrometry technique (Cho et al.,
99 2014). They found that the addition of OH radicals to the vinyl carbons is dominant,
100 and the determined rate coefficient is $(5.80 \pm 0.49) \times 10^{-11} \text{ cm}^3 \text{ molecule}^{-1} \text{ s}^{-1}$ at room
101 temperature. In the smog chamber experiments, Tajuelo et al., (2019a, 2019b and
102 2019c) found that the SOA yields from the photolysis and photooxidation of styrene
103 and its homologous species increase with the concentration of initial reactants
104 increasing, and benzaldehyde, benzoyl chloride, acetophenone and formaldehyde are
105 expected to be the primary gas phase products. Yu et al. (2022) investigated the
106 formation of SOA from styrene in an indoor chamber under different NO_x and RH
107 conditions, and found the SOA yields decrease with increasing RH in both the H₂O₂
108 and NO_x systems. The C₇ and C₈ species are the main products in the H₂O₂ system,
109 while organic nitrates are the major components in the NO_x system. Although the
110 possible molecular formula and chemical composition of the oxidation products from
111 the reaction styrene + OH are given in the aforementioned studies, the specific
112 molecular structures and formation pathways remain ambiguous. Additionally, to the

113 best of our knowledge, the majority of studies mainly focus on the first
114 generation OH oxidation products to date, while the formation mechanisms of
115 multifunctional products from the multi-generation OH oxidation of styrene are still
116 limited.

117 In the present study, the multi-generation OH oxidation mechanisms of styrene
118 in the presence of HO₂ /NO are investigated using the quantum chemistry methods.
119 The calculated results arising from the first generation OH oxidation reactions are
120 presented herein for comparison with the available literatures to ascertain the
121 reliability of the employed theoretical method. For the multi-generation OH
122 oxidation reactions of styrene, all the possible pathways, including H-abstraction,
123 OH-addition, O₂-addition, cyclization, ring-opening, intramolecular H-shifts, C-C
124 bond and O-O bond scission, and HO₂-elimination, are taken into account.
125 Additionally, the saturated concentrations of the formed multifunctional products are
126 estimated to identify the volatility classes.

127 **2. Computational methods**

128 **2.1 Electronic structures and energy calculations**

129 The electronic structures and energy calculations of all stationary points,
130 including reactants (R), intermediates (IM), transition states (TS) and products (P), are
131 performed using the Gaussian 16 program (Frisch et al., 2016). Geometric
132 optimizations of all stationary points on the potential energy surfaces (PESs) are
133 carried out at the M06-2X/6-31+g(d,p) level of theory, since it has reliable
134 performance for describing the noncovalent interactions, thermochemical, and
135 kinetics (Zhao and Truhlar, 2008). Harmonic vibrational frequencies are determined at
136 the M06-2X/6-31+g(d,p) theoretical level to confirm the characteristics of all
137 stationary points (a local minimum or a saddle point). The zero-point vibrational
138 energy (ZPVE) is scaled by a factor of 0.967 (Alecú et al., 2010). Intrinsic reaction
139 coordinate (IRC) calculations are carried out to ascertain the connection of the given
140 TS between the designated local minima R and P (Fukui, 1981). Single point energy
141 calculations are performed at the M06-2X/6-311++G(3df,3pd) level based on the

142 M06-2X/6-31+g(d,p) optimized geometries.

143 In order to further evaluate the reliability of the computational method employed
144 herein, the single point energies of all the stationary points involved in the initial
145 addition of OH radicals to styrene and intramolecular H-shift reactions of the first
146 generation peroxy radicals S2-1-x are recalculated using the DLPNO-CCSD(T)/
147 aug-cc-pVTZ method performed using the Orca 6.1 program (Neese, 2025). As shown
148 in Table S1, the ΔE_a values obtained using the M06-2X/6-311++G(3df,3pd) method
149 are consistent with those derived from the DLPNO-CCSD(T)/aug-cc-pVTZ method.
150 The largest deviation and the average absolute deviation are 1.2 and 0.6 kcal/mol,
151 respectively, indicating that the computational method employed in this study is
152 reliable. Considering the computational cost, the M06-2X/6-311++G(3df,3pd) method
153 is employed to investigate the formation mechanism of multifunctional products from
154 the multi-generation OH oxidation of styrene. The energy barrier (ΔE_a) and reaction
155 energy (ΔE_r) are defined as the difference in energy between TS and IM, as well as
156 between P and R.

157 **2.2 Conformer research**

158 RO₂ radicals formed from the addition of O₂ to the carbon-centered site of alkyl
159 radicals R have multiple possible conformers due to the different orientations of O₂
160 attack (Chen et al., 2021; Fu et al., 2020; Møller et al., 2016 and 2020). An initial
161 structure of RO₂ radicals is optimized at the B3LYP/6-31+G(d) level and
162 subsequently used as the starting geometry to perform the conformer search
163 conducted using the Molclus program (Lu, 2024). The resulting structures are initially
164 optimized at the B3LYP/6-31+G(d) level, as this method accurately predicts the
165 relative energy ordering of different conformers (Møller et al., 2016 and 2020). For
166 the intramolecular H-shift reactions of RO₂ radicals, the lengths of the O-O, C-H and
167 O-H bonds in the conformational sampling of TSs are constrained to retain the cyclic
168 TS structure. All unique conformers of R, TS and P within 5.0 kcal/mol with respect
169 to the lowest energy conformer are further optimized at the M06-2X/6-31+g(d,p) level
170 of theory. Then, the single point energy calculations are performed at the

171 M06-2X/6-311++G(3df,3pd) level of theory. RO radicals formed by the bimolecular
172 reactions of RO₂ radicals with HO₂ radicals and NO also have multiple conformers. In
173 order to obtain the lowest energy conformer, a similar methodology is employed in
174 the present study.

175 2.3 Kinetics calculations

176 The rate coefficients of unimolecular reactions, including intramolecular H-shifts,
177 cyclization, HO₂-elimination, and C-C bond and C-O bond scissions, are calculated
178 using the RRKM theory along with energy-grained master equation (RRKM-ME)
179 (Holbrook et al., 1996). The rate coefficients of bimolecular reactions, involving
180 H-abstraction and OH-addition, are determined using the traditional transition state
181 theory (TST) (Fernández-Ramos et al., 2007). An asymmetric one-dimensional Eckart
182 model (Eckart, 1930) is employed to consider the tunneling correction factors in the
183 rate coefficient calculations based on RRKM-ME and TST. A single exponential down
184 model in the RRKM-ME calculations is utilized to approximate the collision transfer
185 ($\langle \Delta E \rangle_{\text{down}} = 200 \text{ cm}^{-1}$). The Lennard-Jones parameters of all intermediate species are
186 estimated using the empirical formula as proposed by Gilbert and Smith (1990).

187 For the intramolecular H-shifts of RO₂ and RO radicals, the rate coefficients are
188 computed using the multiconformer transition state theory (MC-TST) (Møller et al.,
189 2016), which is expressed as Eq. (1): (Møller et al., 2016 and 2020; Pasik et al., 2024)

$$190 \quad k_{\text{MC-TST}} = \kappa \frac{k_{\text{B}}T}{h} \frac{\sum_i^{\text{TS conf.}} \exp\left(\frac{-\Delta E_i}{k_{\text{B}}T}\right) Q_{\text{TS},i}}{\sum_j^{\text{R conf.}} \exp\left(\frac{-\Delta E_j}{k_{\text{B}}T}\right) Q_{\text{R},j}} \exp\left(-\frac{E_{\text{TS}} - E_{\text{R}}}{k_{\text{B}}T}\right) \quad (1)$$

191 where κ is the Eckart tunneling coefficient, h is Planck's constant, k_{B} is
192 Boltzmann's constant, and T is the absolute temperature (298.15 K). $Q_{\text{TS},i}$ and $Q_{\text{R},j}$
193 refer to the partition functions of the corresponding transition state i and reactant j
194 conformers, respectively. ΔE_i and ΔE_j represent the relative electronic energies
195 between the corresponding transition state i and reactant j conformers and the lowest
196 energy conformers, respectively. E_{TS} and E_{R} stand for the electronic energies of the
197 lowest energy transition state and reactant conformers, respectively. All kinetics
198 calculations are carried out using the KiSThelP 2021 and MESMER 6.0 programs

199 (Glowacki et al., 2012; Canneaux et al., 2013).

200 **3. Results and discussion**

201 **3.1 First generation OH oxidation mechanisms of styrene**

202 Styrene is composed of a benzene ring and a vinyl group, and its oxidation
203 initiated by OH radicals may proceed either on the vinyl group or on the benzene ring.
204 Previous literature has demonstrated that the addition of OH radicals to terminal
205 carbon (C_{β} -site) of a vinyl group in styrene is the dominant pathway, with the
206 branching ratio of 88.2% (Wu et al., 2021). Therefore, the C_{β} -site OH-addition
207 reaction is mainly considered in the present study. Figure 1 depicts that this reaction
208 starts with the formation of a pre-reactive complex IM1, and then transforms into an
209 alkyl radical S1-1 via transition state TS1 with a ΔE_a of 0.8 kcal/mol. The rate
210 coefficient of C_{β} -site OH-addition reaction is estimated to be $1.5 \times 10^{-11} \text{ cm}^3$
211 $\text{molecule}^{-1} \text{ s}^{-1}$ at ambient temperature, which is approximately consistent with the
212 experimental ($1.2\text{-}6.2 \times 10^{-11} \text{ cm}^3 \text{ molecule}^{-1} \text{ s}^{-1}$) and theoretical values ($1.7\text{-}2.0 \times$
213 $10^{-11} \text{ cm}^3 \text{ molecule}^{-1} \text{ s}^{-1}$) for the total rate coefficient of the reaction styrene + OH
214 (Wu et al., 2021; Zhang et al., 2024).

215 Due to the existence of resonance structures with radical character on the
216 aromatic ring, the resulting S1-1 can readily isomerize into three other species,
217 namely, S1-2, S1-3 and S1-4. The attack of an O_2 molecule on the C-center site of
218 S1-1 leads to the formation of the first generation peroxy radicals S2-1-x ($\Delta E_r > -59.6$
219 kcal/mol). The formed S2-1-x includes eight energetically similar conformers due to
220 the different orientations of O_2 attack. In order to distinguish the different conformers,
221 the subscript letter x is used in the present study. The energy ordering of different
222 conformers follows an alphabetical sequence, in which letter a denotes the lowest
223 energy conformer. The Boltzmann population of different conformers in S2-1-x is
224 listed in Table S2.

225 For the unimolecular decomposition reactions of S2-1-x, there are three kinds of
226 pathways. One is the intramolecular H-shift reactions, where the hydrogen atom
227 migrates from the $-\text{CH}_2$, $-\text{CH}$ and $-\text{OH}$ groups to the terminal oxygen atom of the –

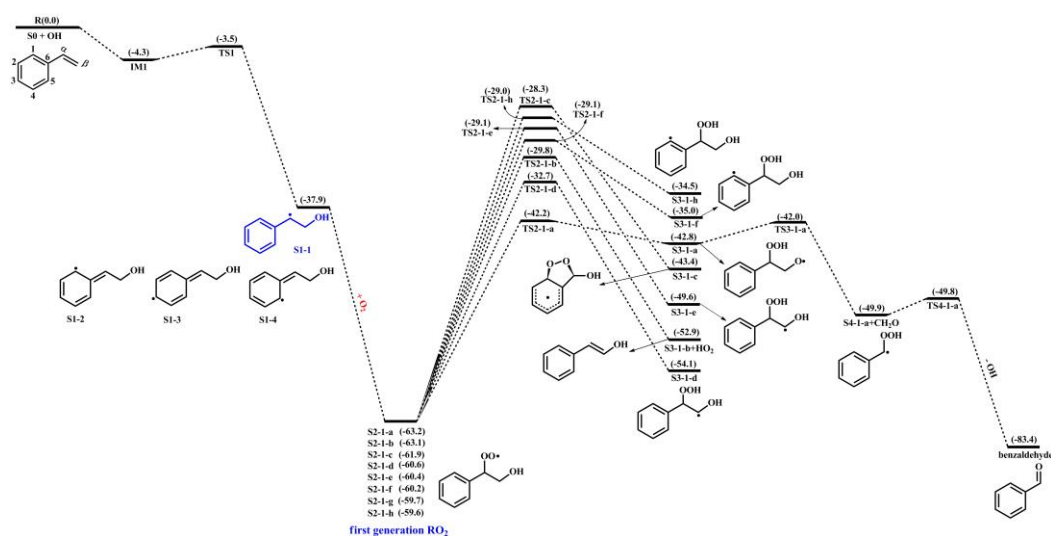
228 OO group leading to various alkyl and alkoxy radicals. Among these competing
229 H-shift reactions, the hydrogen atom at the –OH group can be transferred via a
230 six-membered ring transition state (1,5-H shift) to yield an alkoxy radical S3-1-a,
231 which exhibits the lowest barrier ($\Delta E_a = 21.0$ kcal/mol). The resulting S3-1-a can
232 undergo the C_α - C_β bond cleavage to produce a formaldehyde and an alkyl radical
233 S4-1-a ($\Delta E_a = 0.8$ kcal/mol), followed by an OH radical release to form benzaldehyde
234 ($\Delta E_a = 0.1$ kcal/mol). The rate coefficients for the aforementioned three pathways are
235 calculated to be 2.7×10^{-4} , 4.6×10^{10} and $7.2 \times 10^{10} \text{ s}^{-1}$, respectively. Based on the
236 values of ΔE_a and the corresponding rate coefficients, it can be concluded that the
237 1,5-H shift reaction is the rate-determining step in the formation of benzaldehyde. The
238 other is the cyclization, where the –OO group attacks the C=C double bond in the
239 benzene ring forming a cyclic peroxide alkyl radical S3-1-c ($\Delta E_a = 33.6$ kcal/mol).
240 The last is the HO₂-elimination, where a concerted process of C_α -O and C_β -H bonds
241 scission forms a closed-shell species S3-1-b and a HO₂ radical byproduct ($\Delta E_a = 33.3$
242 kcal/mol). The aforementioned results show that the cyclization and HO₂-elimination
243 reactions are less important due to their higher barriers.

244 As depicted in Figure S1, the formations of the first generation peroxy radicals
245 S2-2-x from the association reaction S1-2 + O₂ are strongly endothermic ($\Delta E_r =$
246 8.1-10.4 kcal/mol), suggesting that they have a significant potential to redissociate
247 back to reactants S1-2 and O₂. The resulting S2-2-x can undergo through various
248 intramolecular H-shifts to yield distinct C-centered and O-centered radicals. Among
249 these competing H-shift pathways, hydrogen transfer from the –OH group to the
250 terminal oxygen of –OO group has the lowest barrier ($\Delta E_a = 17.4$ kcal/mol). A similar
251 conclusion is also obtained from the association reactions S1-3 + O₂ ($\Delta E_r = 6.6$ - 7.1
252 kcal/mol) and S1-4 + O₂ ($\Delta E_r = 8.1$ - 11.1 kcal/mol) that the formations of the first
253 generation peroxy radicals S2-3-x and S2-4-x are thermochemically unfavorable, and
254 their subsequent intramolecular H-shift barriers are considerably high (Figures S2 and
255 S3). Therefore, in the present study, we mainly focus on the subsequent reaction
256 mechanisms of S2-1-x under both low and high NO_x conditions.

257 In the low-NO_x conditions, the bimolecular reaction with HO₂ radicals is
258 expected to be the dominant sink for RO₂ radicals (Orlando and Tyndall, 2012;
259 Vereecken et al., 2015). Previous studies have reported that the rate coefficient
260 $k_{\text{RO}_2+\text{HO}_2}$ for the reactions of alkyl peroxy radicals with HO₂ radicals is 1.7×10^{-11}
261 $\text{cm}^3 \text{ molecule}^{-1} \text{ s}^{-1}$ (Atkinson and Arey, 2003; Boyd et al., 2003). The typical
262 atmospheric concentration of HO₂ radicals is 20-40 pptv (Wang et al., 2017; Bianchi
263 et al., 2019), resulting in the pseudo-first-order rate constant $k'_{\text{RO}_2+\text{HO}_2} = k_{\text{RO}_2+\text{HO}_2}$
264 $[\text{HO}_2]$ of 0.01-0.02 s^{-1} . The isomerization reaction of RO₂ radicals is competitive with
265 the bimolecular reactions with HO₂ radicals only when the rate coefficient of
266 intramolecular H-shifts exceeds 0.01-0.02 s^{-1} . In the high-NO_x conditions, the
267 bimolecular reaction of RO₂ radicals with NO is considered to be a dominant sink
268 (Orlando and Tyndall, 2012; Vereecken et al., 2015). The rate coefficient $k_{\text{RO}_2+\text{NO}}$ for
269 the reaction of alkyl peroxy radicals with NO is determined to be $9.0 \times 10^{-12} \text{ cm}^3$
270 $\text{molecule}^{-1} \text{ s}^{-1}$ (Atkinson and Arey, 2003; Bianchi et al., 2019). The typical
271 atmospheric concentration of NO is 0.4-40 ppbv (Wang et al., 2017; Bianchi et al.,
272 2019), leading to the pseudo-first-order rate constant $k'_{\text{RO}_2+\text{NO}} = k_{\text{RO}_2+\text{NO}} [\text{NO}]$ of
273 0.1-10 s^{-1} . The intramolecular H-shift reaction of RO₂ radicals can compete with the
274 bimolecular reaction with NO only when the rate coefficient of the former case
275 exceeds 10 s^{-1} . Therefore, we use the $k'_{\text{RO}_2+\text{HO}_2}$ (0.01-0.02 s^{-1}) and $k'_{\text{RO}_2+\text{NO}}$ (0.1-10 s^{-1})
276 values as thresholds to evaluate the relative importance of the isomerization reactions
277 of RO₂ radicals under both low- and high-NO_x conditions. Previous studies have also
278 employed the same methodology to evaluate the relative importance of isomerization
279 and bimolecular reactions of RO₂ radicals during the OH-initiated oxidation of
280 organophosphate esters and alkylbenzenes (Wang et al., 2017; Fu et al., 2024). For the
281 intramolecular H-shift reactions of S2-1-x, the rate coefficient $k_{\text{MC-TST}}$ is estimated to
282 be $1.6 \times 10^{-4} \text{ s}^{-1}$, which is 2-4 orders of magnitude lower than $k'_{\text{RO}_2+\text{HO}_2}$ and $k'_{\text{RO}_2+\text{NO}}$,
283 indicating that the isomerization reaction of S2-1-x is less competitive than the
284 bimolecular reactions with HO₂ radicals and NO.

285 In the presence of NO, the bimolecular reactions of S2-1-x with NO initially
286 proceed via oxygen-to-oxygen coupling to yield organic nitrites ROONO, which

287 subsequently decompose into benzaldehyde and CH₂OH radical or isomerize to
 288 organic nitrates RONO₂. The energy barrier of the rate-limiting step predicted in
 289 Wang's study for the formation of benzaldehyde is 28.4 kcal/mol, which is
 290 approximately 4.0 kcal/mol greater than that for the formation of RONO₂ (Wang et al.,
 291 2015). In the absence of NO, the hydroperoxides ROOH formed from the bimolecular
 292 reaction of S2-1-x with HO₂ radicals are anticipated to be the dominate products. The
 293 aforementioned results are further confirmed by the recent smog chamber experiment
 294 study that C₇ and C₈ series products, as well as organic nitrates are the main
 295 components of SOA in the OH-initiated oxidation of styrene under different NO_x
 296 conditions (Yu et al., 2022). Considering that the extensive studies on the OH-initiated
 297 oxidation of benzaldehyde have done (Sebbar et al., 2011; Zhao et al., 2022; Iuga et
 298 al., 2008), this study primarily focuses on the multi-generation OH oxidation
 299 mechanisms of ROOH and RONO₂ under both low- and high-NO_x conditions.



300

301 **Figure 1.** PES for the first-stage oxidation of styrene initiated by OH radicals and the
 302 isomerization reactions of S2-1-x at the M06-2X/6-311++G(3df,3pd)//M06-2X/6-31+g(d,p) level

303 **3.2 Second generation OH oxidation mechanisms of 1st-ROOH** 304 **and 1st-RONO₂**

305 The first generation products, including hydroperoxides 1st-ROOH and organic
 306 nitrates 1st-RONO₂, include multiple conformers. To obtain the global minimum of
 307 1st-ROOH and 1st-RONO₂, the conformer search is performed by using the Molclus
 308 program. The resulting structures are initially optimized at the M06-2X/6-31+g(d,p)

309 level, then the single point energies are calculated at the M06-2X/6-311++G(3df,3pd)
310 level. The global minimum structures of 1st-ROOH (S4) and 1st-RONO₂ (S5) are
311 presented in Figure S4.

312 **3.2.1 The oxidation mechanism of 1st-ROOH initiated by OH** 313 **radicals**

314 The reaction 1st-ROOH (S4) + OH proceeds through the addition of OH radicals
315 to either side of the benzene ring to yield various alkyl radicals, as depicted in Figure
316 2. In the present study, *syn*-OH-addition is defined as the scenario in which the
317 addition of OH radicals occurs at the same side as the –OOH group, while
318 *anti*-OH-addition is referred to the scenario in which the addition of OH radicals
319 occurs at the opposite side as the –OOH group. For the *syn*-OH-addition reactions, the
320 addition of OH radicals to the C1-site of 1st-ROOH (S4) exhibits the lowest barrier
321 ($\Delta E_a = 3.6$ kcal/mol) due to the stability of the formed product, P_{S4-add1}'. A similar
322 conclusion is also obtained from the *anti*-OH-addition reactions that the OH-addition
323 pathway occurring at the C1-site is favorable ($\Delta E_a = 0.8$ kcal/mol). Notably, the
324 preferred OH-addition pathway in the *anti*-OH-addition reactions exhibits greater
325 competitiveness compared to that in the *syn*-OH-addition reactions. It can be
326 explained by the greater steric hindrance present in the latter reaction. In order to
327 further evaluate the reliability of our results, ΔE_a of all the *syn*-OH-addition and
328 *anti*-OH-addition reactions are recalculated using the DLPNO-CCSD(T)/
329 aug-cc-pVTZ//M06-2X/6-311+G(d,p) method. As shown in Table S3, the ΔE_a values
330 obtained using the M06-2X/6-311++G(3df,3pd) method are in good agreement with
331 those derived from the DLPNO-CCSD(T)/aug-cc-pVTZ method. The largest
332 deviation and the average absolute deviation are 1.2 and 0.9 kcal/mol, respectively,
333 indicating that the M06-2X/6-311++G(3df,3pd) method employed in this study is
334 reliable. Based on the values of ΔE_a obtained using the DLPNO-CCSD(T)/
335 aug-cc-pVTZ method, it can also be concluded that the addition of OH radicals to
336 C1-site, occurring at the opposite direction relative to the –OOH group, is
337 energetically favorable. The rate coefficients of the addition of OH radicals to the

338 different sites of 1st-ROOH are calculated to be 8.2×10^{-12} (C1-site), 5.8×10^{-15}
339 (C2-site), 8.3×10^{-15} (C3-site), 8.6×10^{-15} (C4-site), 2.7×10^{-12} (C5-site) and $4.1 \times$
340 10^{-13} (C6-site) $\text{cm}^3 \text{ molecule}^{-1} \text{ s}^{-1}$, respectively. The branching ratios for OH addition
341 to the C1, C5 and C6 sites are predicted to be 72.4%, 23.8% and 3.6%, respectively,
342 while the sum of branching ratios for OH addition to other carbon sites is less than
343 1%.

344 Our result is opposite to Zhang's finding that the addition of OH radicals to
345 C6-site would be the most favorable pathway (Zhang et al., 2024). The discrepancy
346 can be explained by the following three factors: (1) The 1st-ROOH conformer selected
347 in the Zhang's study is not the global minimum. In the present study, the global
348 minimum conformer of 1st-ROOH, identified through the conformer search, is found
349 to be 2.2 kcal/mol lower than the 1st-ROOH structure selected in the Zhang's study. (2)
350 The pre-reactive complexes are not considered in the Zhang's study. The addition of
351 OH radicals to C1-, C2-, C3- and C6-sites, occurring at the opposite direction relative
352 to the -OOH group, are merely considered in the Zhang's study. They found that the
353 apparent energy barrier of the addition of OH radicals to C6-site is smallest, and is
354 therefore expected to be the favorable pathway. Actually, these OH-addition reactions
355 are modulated by the pre-reactive complexes. It may be inappropriate to determine the
356 favorable pathway based solely on apparent activation energy without considering the
357 pre-reaction complexes. (3) From a geometric perspective, the addition of OH radicals
358 to C6-site is associated with greater steric hindrance compared to other sites, as
359 C6-atom connects with a larger functional group. Base on the aforementioned
360 discussions, we believe that the addition of OH radicals to C6-site is unlikely to be the
361 dominant pathway. Our calculations also confirm that the addition of OH radicals to
362 C6-site is less importance compared to that at the C1-site.

363 Our conclusion is further supported by the reaction toluene + OH that the
364 *ortho*-OH-addition reaction exhibits significant dominance, with the branching ratio
365 of up to 69.8-75.8% (Ji et al., 2017; Zhang 2019; Wu et al., 2020). Considering the
366 high reactivity of *ortho*-OH-addition in the reactions toluene + OH and 1st-ROOH
367 (S4) + OH, the substitute effects of the -CH₃ and -OOH groups are explicitly

368 discussed in the present study. Notably, the $-\text{CH}_3$ group in toluene is bonded to the C6
369 atom, and the $-\text{OOH}$ group in 1st-ROOH is bonded to the C α atom, as depicted in
370 Figure S5. The optimized geometries of toluene and 1st-ROOH and the NPA atomic
371 charges of all the carbon atoms in the benzene ring are displayed in Figure S5. The
372 C-C bond lengths and the C-C-C bond angles in the benzene ring of toluene are
373 approximately 1.39 Å and 120°, respectively, which are consistent with those in the
374 benzene ring of 1st-ROOH. The aforementioned results show the effect of the $-\text{CH}_3$
375 and $-\text{OOH}$ groups on the geometric structure of benzene ring is negligible. From the
376 perspective of NPA atomic charges, the charges on the C1 (-0.246 e) and C5 (-0.246 e)
377 atoms are more greater than those on the other carbon atoms in the benzene ring of
378 toluene. And the OH-adduct formed from the *ortho*-OH-addition reaction exhibits the
379 greater stability. These results indicate that the $-\text{CH}_3$ group is a typical *ortho*-directing
380 substituent and exerts an activating effect on the *ortho*-site of the benzene ring, which
381 explains why the *ortho*-OH-addition reaction is predominant in the reaction toluene
382 + OH. Compared with the charges on the carbon atoms in the benzene ring of toluene,
383 the charges on C1 and C6 atoms increase by 0.013 e and 0.057 e, respectively, in
384 1st-ROOH, which can be attributed to the electron-withdrawing effect of the $-\text{OOH}$
385 group. The charge on the C1 atom (-0.259 e) is the highest, and the stability of the
386 resulting OH-adduct is the greatest, implying that the addition of OH radicals to
387 C1-site is dominant in the reaction 1st-ROOH + OH. Therefore, a direct comparison
388 of the favorable OH-addition pathway in the reactions toluene + OH and 1st-ROOH
389 (S4) + OH is performed in this study.

390 The formed product P_{S4-add1} includes two conjugate double bonds (C₂=C₃ and
391 C₄=C₅), which can readily isomerize to P_{S4-add2} and P_{S4-add3}, as evident from Figure S6.
392 In the present of O₂, the attack of an O₂ molecule on the C-centered site of P_{S4-add1},
393 P_{S4-add2}, and P_{S4-add3} proceed via the barrierless processes to produce the second
394 generation peroxy radicals P_{S4-add1-a/-s}, P_{S4-add2-a/-s} and P_{S4-add3-a/-s}. The O₂-addition
395 reaction occurring at the same direction as the $-\text{OOH}$ group is defined as
396 *syn*-O₂-addition, while the O₂-addition reaction occurring at the opposite direction as
397 the $-\text{OOH}$ group is defined as *anti*-O₂-addition. For the reaction P_{S4-add1} + O₂ →

398 $P_{S4-add1-a/-s}$, ΔE_r of *anti*-O₂-addition is -5.8 kcal/mol, which is lower than that of
399 *syn*-O₂-addition by 0.4 kcal/mol, suggesting that *anti*-O₂-addition is preferable over
400 *syn*-O₂-addition in energy. For the reactions $P_{S4-add2} + O_2 \rightarrow P_{S4-add2-a/-s}$ and $P_{S4-add3} +$
401 $O_2 \rightarrow P_{S4-add3-a/-s}$, it can be concluded the same by the ΔE_r values that
402 *anti*-O₂-addition reaction is energetically feasible.

403 The resulting $P_{S4-add1-a/-s}$ can proceed intramolecular cyclization reaction, where
404 the attack of end-site oxygen atom of the -OO group on C2-site of the C₂=C₃ double
405 bond, leading to the formation of peroxide bicyclic alkyl radicals. ΔE_a and ΔE_r of the
406 reaction $P_{S4-add1-a} \rightarrow P_{S4-add1-a-1}$ are 11.8 and -16.8 kcal/mol, respectively, which are
407 lower than those of the reaction $P_{S4-add1-s} \rightarrow P_{S4-add1-s-1}$ by 3.9 and 2.2 kcal/mol,
408 respectively. The aforementioned results reveal that the intramolecular cyclization
409 reaction of *anti*-O₂-addition product $P_{S4-add1-a}$ is favorable on both thermochemically
410 and kinetically. A similar conclusion is also derived from the intramolecular
411 cyclization reactions of *anti*-O₂-addition products $P_{S4-add2-a}$ and $P_{S4-add3-a}$. Notably, the
412 barriers of the intramolecular cyclization reactions $P_{S4-add2-a} \rightarrow P_{S4-add2-a-1}$ ($\Delta E_a =$
413 31.1 kcal/mol) and $P_{S4-add2-a} \rightarrow P_{S4-add2-a-2}$ ($\Delta E_a = 34.6$ kcal/mol) are extremely high,
414 making them insignificant in the atmosphere. The tautomerization between
415 $P_{S4-add1-a-1}$ and $P_{S4-add3-a-1}$ readily occurs due to the existence of resonance structures,
416 and it is therefore that the latter conformer is selected as a prototype for the
417 investigating of its subsequent reaction mechanism.

418 The formed $P_{S4-add3-a-1}$ can combine with an O₂ molecule leading to the third
419 generation peroxy radicals (also called as peroxide bicyclic peroxy radicals, BPR)
420 $P_{S4-add3-a-2}$, and the lowest energy conformer is presented in Figure S7. The
421 isomerization of $P_{S4-add3-a-2}$ may undergo through a concerted process of the cleavage
422 of -O-O- bridge bond and C₁-C₂ bond as well as hydrogen atom transfer from the
423 hydroxyl group to the bridge oxygen atom, yielding a new peroxy radical ($\Delta E_a = 28.5$
424 kcal/mol). The room temperature rate coefficient is calculated to be $3.0 \times 10^{-9} \text{ s}^{-1}$,
425 which is several orders of magnitude low than the typical pseudo-first-order rate
426 constants $k'_{RO_2+HO_2}$ (0.01-0.02 s⁻¹) and k'_{RO_2+NO} (0.1-10 s⁻¹), suggesting that the
427 isomerization reaction is less importance in the atmosphere. Therefore, the

428 bimolecular reactions of $P_{S4-add3-a-2}$ with HO_2 radicals with NO are mainly taken into
429 consideration in this study.

430 In the pristine environments, $P_{S4-add3-a-2}$ can react with HO_2 radicals resulting in
431 the formation of the second generation products, bicyclic hydroperoxide 2nd-ROOH
432 (S6) and peroxide bicyclic alkoxy radical (BAR) $P_{S4-add3-a-3}$, as depicted in Figure S7.
433 For the subsequent reactions of S6 initiated by OH radicals, the detailed mechanisms
434 are discussed in Section 3.3.1. From Figure 3, it can be seen that the unimolecular
435 decomposition of $P_{S4-add3-a-3}$ involves two kinds of pathways. One is the ring-opening
436 reaction, where the breakage of C_5-C_6 bond produces an alkyl radical S7 ($\Delta E_a = 5.9$
437 kcal/mol.). The other is cyclization reaction, where the attack of oxygen atom of
438 O-centered site on the C4-site of the $C_3=C_4$ double bond generates the ring-retaining
439 alkyl radical S15 ($E_a = 8.0$ kcal/mol). The branching ratios for the formation of S7 and
440 S15 are predicted to be 74.7% and 25.3%, respectively.

441 As shown in Figure 3, S7 decomposes through the barrierless rupture of -O-O-
442 bridge bond to form alkoxy radical S8-x, which includes five possible conformers as
443 presented in Figure S8. The Boltzmann populations of different conformers are listed
444 in Table S4. S8-x can undergo various intramolecular H-shifts, in which a hydrogen
445 atom is transferred from different carbon atoms to O-centered site, forming the alkyl
446 radicals. Among the competing H-shift reactions, 1,5 H-shift occurring at the -
447 $C_5(O)H$ group exhibits the smallest barrier ($\Delta E_a = 0.6$ kcal/mol), and k_{MC-TST} is
448 calculated to be $8.2 \times 10^9 s^{-1}$ at ambient temperature (Table S5). The formed S8-c-P
449 can readily isomerize to S9 due to its resonance stabilized structure. The unimolecular
450 decomposition of S9 can proceed through the C1-C2 bond scission to produce a
451 ketene-enol S10 and an alkyl radical S10-1 ($\Delta E_a = 16.1$ kcal/mol), followed by
452 reaction with O_2 leading to a HO_2 radical and a 1,2-dicarbonyl compound S10-2 (ΔE_a
453 = 14.0 kcal/mol). Alternatively, S9 may undergo via the elimination of CO to generate
454 an alkyl radicals S11 ($\Delta E_a = 29.4$ kcal/mol). The aforementioned results show that the
455 formation of S10 and S10-1 is energetically favorable, with the rate coefficient k_{S10} of
456 $26.1 s^{-1}$.

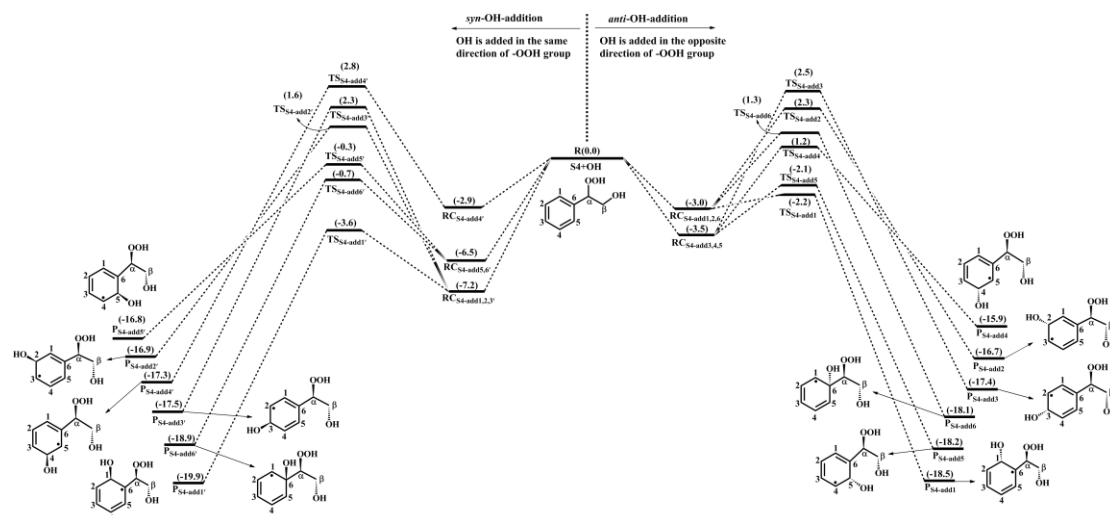
457 In the presence of O_2 , the attack of an O_2 molecule on the C-centered sites of S9

458 leads to the fourth generation peroxy radical S12-x ($\Delta E_r > -20.5$ kcal/mol). Adopting
459 the rate coefficient k_{R+O_2} of 6.0×10^{-12} cm³ molecule⁻¹ s⁻¹ for the reactions of alkyl
460 radicals with O₂, and the atmospheric O₂ concentration of 5×10^{18} molecule cm⁻³ (Ma
461 et al., 2021), the pseudo-first-order rate constant $k'_{R+O_2} = k_{R+O_2} [O_2]$ is 3.0×10^7 s⁻¹.
462 The unimolecular decomposition of alkyl radicals is competitive only when their
463 decay rate exceeds 3.0×10^7 s⁻¹. k'_{R+O_2} is about six orders of magnitude greater than
464 k_{S10} , indicating that the unimolecular decomposition of S9 is less importance. As
465 shown in Figure S9, S12-x can proceed various intramolecular H-shift reactions,
466 where hydrogen atom migrates from the different carbon sites or hydroxyl groups to
467 the terminal oxygen atom of the -OO group, resulting in the formation of QOOH
468 radicals and alkoxy radicals. Among these competing H-shift reactions, the 1,7-H
469 transfer at the C α -site leading to the formation of S12-d-P exhibits the smallest barrier
470 ($\Delta E_a = 17.4$ kcal/mol). Then, it decomposes to yield an OH radical and a closed-shell
471 product S13 containing a hydroperoxide, three hydroxyl and three carbonyl groups
472 ($\Delta E_a = 1.1$ kcal/mol).

473 S8-x can proceed through the C₁-C₂ bond scission to yield an unsaturated
474 1,4-dicarbonyl species S14 and an alkyl radical S10-1 ($\Delta E_a = 2.2$ kcal/mol), with the
475 rate coefficient of 2.1×10^{10} s⁻¹. Notably, both the 1,5 aldehyde H-shift and C₁-C₂
476 bond scission reactions yield a closed-shell species S10-2 with up to five oxygen
477 atoms, and the branching ratios are predicted to be 28.1% and 71.9%, respectively.
478 The result is further supported by the previous study that the proportion of aldehyde
479 H-shift products constitutes about one third of the total products in the reaction
480 benzene + OH (Wang et al., 2020).

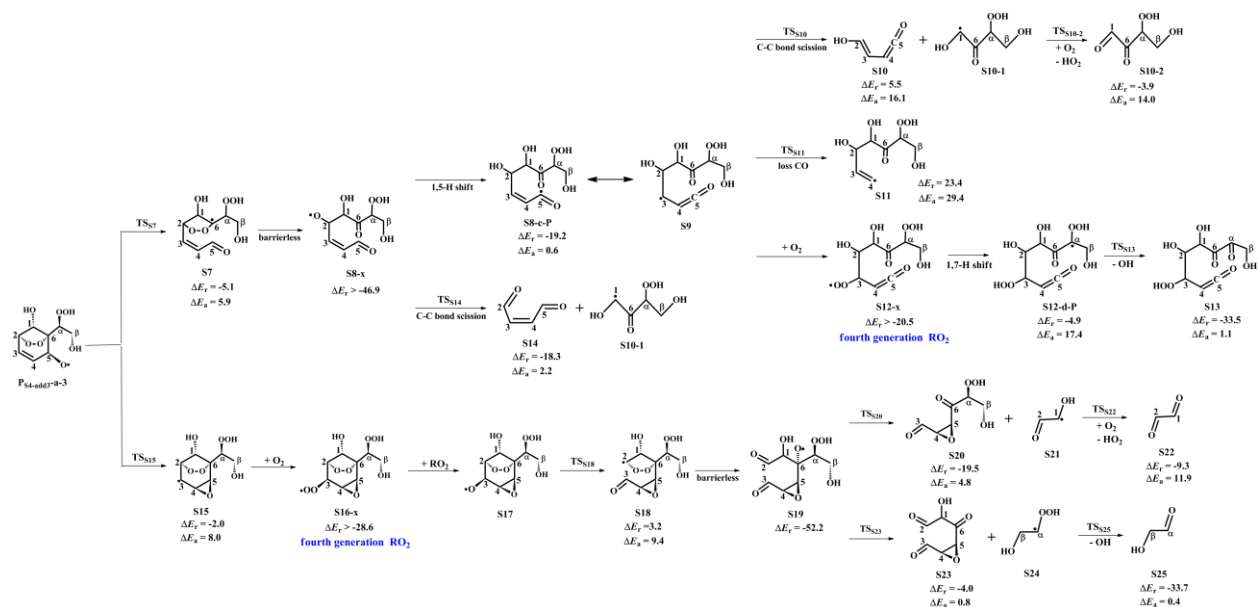
481 As shown in Figure 3, S15 can further react with O₂ leading to the fourth
482 generation peroxy radical S16-x, which can proceed either intramolecular H-shifts
483 forming QOOH radicals (Figure S10), or reactions with RO₂ radicals and NO forming
484 alkoxy radical S17. Notably, the barriers of intramolecular H-shifts are extremely
485 high ($\Delta E_a > 34.6$ kcal/mol), making them less importance in the atmosphere. The
486 transformation of S17 undergoes through the breakage of C₂-C₃ bond to produce an
487 alkyl radical S18 ($\Delta E_a = 9.4$ kcal/mol), followed by fragmentation into an alkoxy

488 radical S19 via the barrierless rupture of the -O-O- bridge bond. Then, S19 dissociates
 489 to an OH radical, a glycolaldehyde S25 and a C₆-epoxide product S23 bearing a
 490 hydroxy and three carbonyl groups, being the dominant pathway. The regeneration of
 491 OH radicals drives the successive autoxidation of styrene, eventually leading to
 492 the production of multifunctional products.



493
 494 **Figure 2.** PES for the oxidation of 1st-ROOH(S4) initiated by OH radicals at the
 495 M06-2X/6-311++G(3df,3pd)/M06-2X/6-31+g(d,p) level

496



497
 498 **Figure 3.** PES for the unimolecular decomposition of P_{S4-add3-a-3} and its subsequent reactions at
 499 the M06-2X/6-311++G(3df,3pd)/M06-2X/6-31+g(d,p) level

500 **3.2.2 The oxidation mechanism of 1st-RONO₂ initiated by OH**
 501 **radicals**

502 The OH-initiated oxidation of 1st-RONO₂ (S5) proceeds through the addition of
503 OH radicals to different carbon sites in the benzene ring to form various alkyl radicals
504 P_{S5-addx}, as depicted in Figure 4. Among the competing OH-addition reactions, the
505 OH-addition reaction at the C1-site, which proceeds on the opposite direction as the –
506 ONO₂ group, has the smallest barrier (R_{S5-add1}, ΔE_a = 0.4 kcal/mol) due to the stability
507 of the formed product P_{S5-add1}. The result again shows that the *ortho*-addition reaction
508 is energetically feasible. P_{S5-add1} may isomerize to two other resonance structures,
509 namely, P_{S5-add2} and P_{S5-add3}. For the reaction P_{S5-add1} + O₂, O₂ may add on either the
510 opposite (*anti*-O₂-addition) or the same direction (*syn*-O₂-addition) relative to the –
511 NO₃ group, leading to the second generation peroxy radicals P_{S5-add1-a} and P_{S5-add1-s}
512 (Figure S11). The exoergicity of these two reactions are -6.7 and -4.4 kcal/mol,
513 respectively, suggesting that the *anti*-O₂-addition reaction is thermochemically
514 favorable. Next, they can isomerize via a cyclization process to yield P_{S5-add1-a-1} and
515 P_{S5-add1-s-1} with the ΔE_a of 13.3 and 18.1 kcal/mol. This result shows that the
516 cyclization reaction of *anti*-O₂-addition product P_{S5-add1-a} is kinetically feasible. A
517 similar conclusion is also obtained from the reaction P_{S5-add3} + O₂ that the formation of
518 *anti*-O₂-addition product P_{S5-add3-a-1} is dominant. Due to the existence of the
519 conjugate double bond, it facilitates the tautomerization between P_{S5-add1-a-1} and
520 P_{S5-add3-a-1}. Therefore, we mainly focus on the subsequent chemistry of P_{S5-add3-a-1} in
521 the present study.

522 P_{S5-add3-a-1} can further react with an O₂ molecule leading to the third generation
523 peroxy radicals P_{S5-add3-a-2}, which include multiple conformers. The lowest energy
524 conformer resulting from conformer search is presented in Figure S12. In urban
525 environments, the bimolecular reaction of P_{S5-add3-a-2} with NO yields the second
526 generation products, a bicyclic organic nitrate 2nd-RONO₂ (S26) and a BAR
527 P_{S5-add3-a-3}, as displayed in Figure S12. The detailed mechanism of OH-initiated
528 oxidation of S26 is discussed in Section 3.3.2. As shown in Figure 5, P_{S5-add3-a-3} can
529 either proceed via a ring opening process to form an alkyl radical S27 (ΔE_a = 7.3
530 kcal/mol), or undergo through a cyclization process to generate an epoxide species
531 S35 (ΔE_a = 8.5 kcal/mol). The branching ratios of these two reactions are predicted to

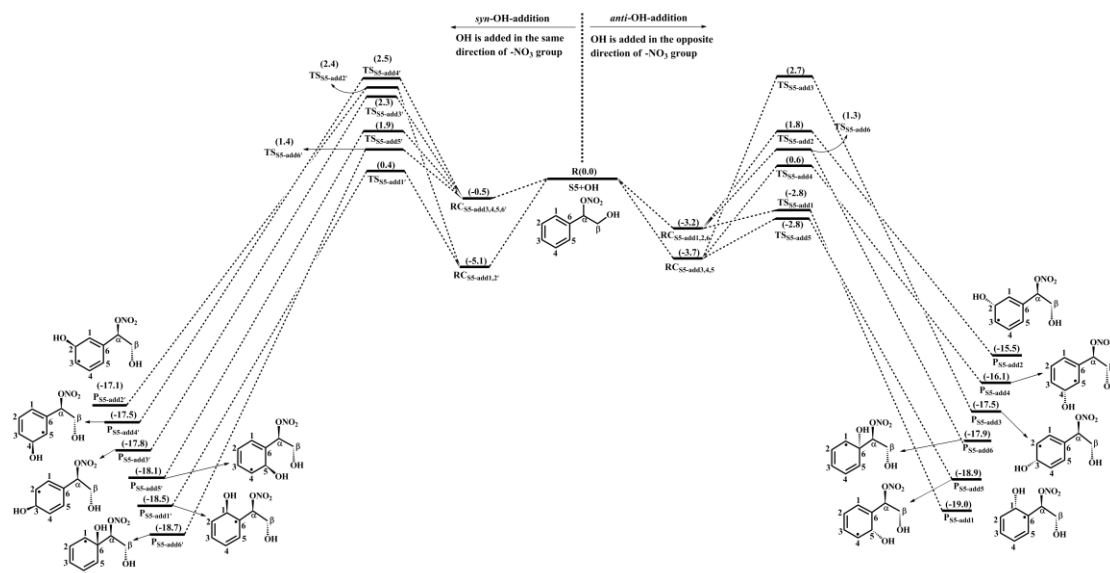
532 be 69.2% and 30.8%, respectively. Notably, the branching ratio of cyclization reaction
533 of P_{S5-add3-a-3} increases by 5.5% compared to that of cyclization reaction of
534 P_{S4-add3-a-3}, suggesting that the –ONO₂ substitution is beneficial to cyclization
535 reaction.

536 The degradation of S27 proceeds through the barrierless scission of -O-O- bridge
537 bond to form S28-x, and the Boltzmann populations of different conformers are listed
538 in Table S6. S28-x can undergo via various intramolecular H-shifts to produce QOOH
539 radicals, in which hydrogen atom transfer from the –C(O)H group to the terminal
540 oxygen atom of the –OO group forming S28-e-P has the smallest barrier ($\Delta E_a = 2.0$
541 kcal/mol) (Figure S13). S28-e-P can readily isomerize to S29, which includes two
542 distinct decomposition pathways. One is the C1-C2 bond cleavage, yielding a
543 ketene-enol S30 and an alkyl radical S30-1 ($\Delta E_a = 17.8$ kcal/mol), followed by
544 reaction with O₂ to form a HO₂ radical and a 1,2-dicarbonyl species S30-2 ($\Delta E_a =$
545 11.7 kcal/mol). The other is the elimination of CO to generate an alkyl radical S31
546 ($\Delta E_a = 24.8$ kcal/mol), but the barrier is considerably high, making this pathway less
547 competitive. The rate coefficient for the formation of S30 and S30-1 is calculated to
548 be 14.4 s⁻¹, which is about six orders of magnitude lower than the pseudo-first-order
549 rate constant k'_{R+O_2} , indicating that the unimolecular decomposition of S29 is
550 insignificant.

551 In the presence of O₂, the bimolecular reaction of S29 with O₂ produces the
552 fourth generation peroxy radicals S32-x, comprising five energetically similar
553 conformers as shown in Figure S14. For the 1,7-H transfer reaction, hydrogen atom at
554 the C α -site can be transferred through an eight-membered ring transition state to
555 generate an alkyl radical S32-d-P ($\Delta E_a = 23.3$ kcal/mol), followed by the elimination
556 of NO₂ forming a closed product S33 ($\Delta E_a = 1.0$ kcal/mol). S33 and S13 are isomeric
557 species, with the former exhibiting more stability than the latter. S28-x can proceed
558 through the cleavage of C₁-C₂ bond to generate an unsaturated 1,4-dicarbonyl
559 compound S34 and an alkyl radical S30-1. The rare coefficients of the 1,5 aldehyde
560 H-shift and C1-C2 bond scission reactions are predicted to be 1.7×10^9 and 5.8×10^9
561 s⁻¹ (Table S7), respectively, with the branching ratios of 23% and 77%. S30-1, formed

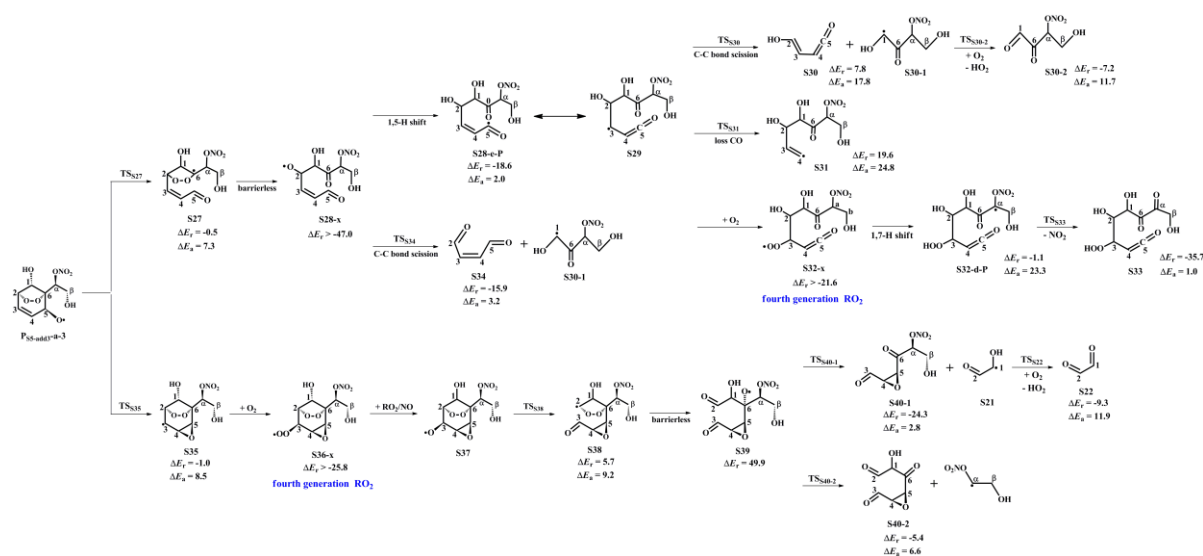
562 from the above mentioned two pathways, may undergo through H-abstraction by O₂
 563 to yield an organic nitrate S30-2 bearing a hydroxyl and two carbonyl groups ($\Delta E_a =$
 564 11.7 kcal/mol).

565 S35 can combine with an O₂ molecule forming the fourth generation peroxy
 566 radicals S36-x, which have five possible conformers as shown in Figure S15. S36-x
 567 can proceed either intramolecular H-shifts forming QOOH radicals, or reaction with
 568 RO₂ radicals and NO generating alkoxy radical S37. However, the barriers of
 569 intramolecular H-shifts are extremely high ($\Delta E_a > 31.3$ kcal/mol), making them less
 570 importance in the atmosphere. The degradation of S37 initially proceeds via the
 571 breakage of C₂-C₃ bond to form S38 ($\Delta E_a = 9.2$ kcal/mol), followed by decomposition
 572 into an alkoxy radical S39 via the barrierless scission of -O-O- bridge bond. The
 573 dominant pathway of the unimolecular decomposition of S39 is the formation of a
 574 glyoxal and a C₆-epoxide species S40-1 bearing a -NO₃, a hydroxyl and two carbonyl
 575 groups. This process differs from the unimolecular decay of S19, where the favorable
 576 pathways is the formation of a tricarbonyl compound S23. The aforementioned results
 577 reveal that the preferable pathway is strongly dependent on the breakage of C-C bond
 578 associated with the property of substituents in the decomposition of alkoxy radicals.



579
 580 **Figure 4.** PES for the oxidation of 1st-RONO₂(S5) initiated by OH radicals at the
 581 M06-2X/6-311++G(3df,3pd)//M06-2X/6-31+g(d,p) level

582



583

584 **Figure 5.** PES for the unimolecular decomposition of P_{55-add3-a-3} and its subsequent reactions at
 585 the M06-2X/6-311++G(3df,3pd)//M06-2X/6-31+g(d,p) level

586 3.3 Third generation OH oxidation mechanisms of 2nd-ROOH 587 and 2nd-RONO₂

588 The second generation products, bicyclic hydroperoxide 2nd-ROOH and bicyclic
 589 organic nitrate 2nd-RONO₂, have multiple possible conformers. The global minimum
 590 structures of 2nd-ROOH (S6) and 2nd-RONO₂ (S26) resulting from the conformer
 591 search are presented in Figures S7 and S12, respectively.

592 3.3.1 The oxidation mechanism of 2nd-ROOH initiated by OH 593 radicals

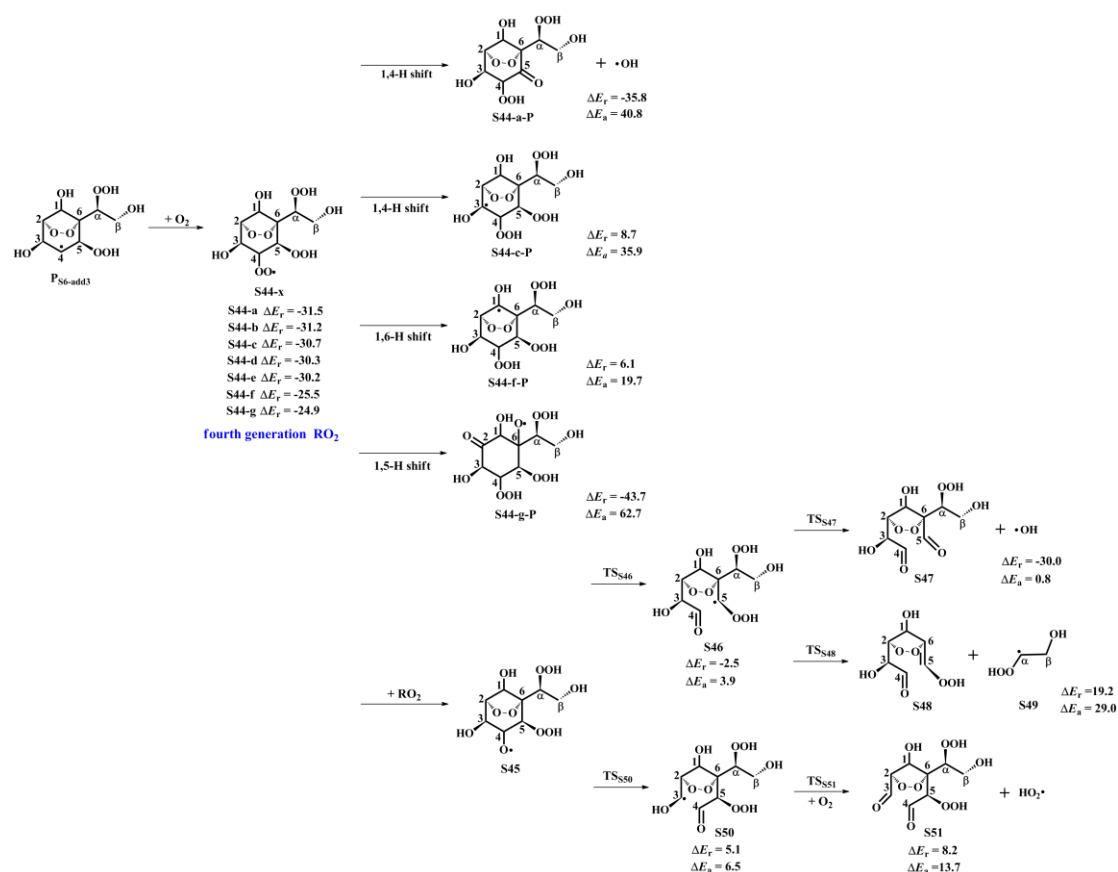
594 OH-initiated oxidation of 2nd-ROOH (S6) can either undergo through the
 595 addition of OH radicals to either side of the C₃=C₄ double bond to generate the alkyl
 596 radicals, or proceed via H-abstraction from the different carbon sites to produce the
 597 alkyl radicals and alkoxy radicals, as shown in Figures S16 and S17. For the
 598 OH-addition reactions, *syn*-OH-addition is defined as the addition of OH radicals on
 599 the same side as the -OOH group, while *anti*-OH-addition is referred to the addition
 600 of OH radicals on the opposite side as the -OOH group. The addition of OH radicals
 601 to the C3-site of the C₃=C₄ double bond forming the product P_{S6-abs3} has the smallest
 602 barrier ($\Delta E_a = 2.4$ kcal/mol) and the exoergicity of -33.5 kcal/mol. For the
 603 H-abstraction reactions, the abstraction of hydrogen atom at the C5-site is the most

604 favorable pathway ($\Delta E_a = 3.6$ kcal/mol) and the exoergicity of -20.2 kcal/mol. It is
605 mainly because that the presence of an allyl group enhances the stability of the
606 resulting product $P_{S6-abs5}$. Notably, the abstraction of hydrogen atom at the C2-site
607 proceeds through a concerted process of C₂-H bond and -O-O- bridge bond rupture,
608 leading to the formation of an alkoxy radical $P_{S6-abs2}$ ($\Delta E_a = 7.2$ kcal/mol). This
609 reaction is expected to be less importance due to its higher energy barrier. The rate
610 coefficient of the favorable OH-addition reaction is calculated to be 6.4×10^{-11} cm³
611 molecule⁻¹ s⁻¹, which is about one order of magnitude greater than that of the
612 preferable H-abstraction reaction (4.1×10^{-12} cm³ molecule⁻¹ s⁻¹). Based on the above
613 discussion, it can be concluded that OH-addition reaction is favorable on both
614 thermochemically and kinetically. This conclusion is further supported by the OH +
615 alkene reaction systems that OH-addition pathways are predominant (Chen et al.,
616 2021; Yang et al., 2017; Arathala and Musah, 2024).

617 As depicted in Figure S18, the unimolecular decay of the product $P_{S6-add3}$
618 resulting from the favorable OH-addition reaction proceeds through a cyclization
619 process to yield an epoxide compound S41 and an OH radical byproduct with the ΔE_a
620 of 15.3 kcal/mol and the rate coefficient k_{R41} of 1.8×10^2 s⁻¹, or undergoes via
621 intramolecular 1,4 H-shift to form a peroxy radical S42 with the ΔE_a of 21.8 kcal/mol
622 and the rate coefficient k_{R43} of 1.9 s⁻¹, or proceeds via the elimination of hydrogen
623 atom to produce an alkene S43 with the ΔE_a of 37.9 kcal/mol. Based on the values of
624 ΔE_a and the corresponding rate coefficients, the dominant pathway of the
625 unimolecular decomposition of $P_{S6-add3}$ is the formation of S41. In the presence of O₂,
626 the pseudo-first-order rate constant k'_{R+O_2} of the reactions of alkyl radicals with O₂ is
627 3.0×10^7 s⁻¹, which is about five orders of magnitude greater than k_{R41} , suggesting
628 that the unimolecular decomposition of $P_{S6-add3}$ is insignificant.

629 As shown in Figure 6, the fourth generation peroxy radicals S44-x formed in the
630 addition reaction $P_{S6-add3} + O_2$ can either proceed via intramolecular H-shifts to form
631 QOOH, or undergo through self- or cross-reactions to yield an alkoxy radical S45.
632 Due to the considerably high barriers of intramolecular H-shifts, they are deemed to
633 be negligible under atmospheric conditions. S45 can convert into an alkyl radical S46

634 through the cleavage of C₄-C₅ bond, or dissociate to an alkyl radical S50 via the
 635 rupture of C₃-C₄ bond. The barrier of the former reaction is 3.9 kcal/mol, which is
 636 lower than that of the latter pathway by 2.6 kcal/mol, indicating that the formation of
 637 S46 is kinetically preferable. Then, S46 decomposes into an OH radical byproduct
 638 and a C₈-product S47 bearing a –OOH, a peroxide bridge, two carbonyls, and three
 639 hydroxy groups, which is expected to be the dominant pathway owing to its lower
 640 barrier. The rate coefficient k_{RS47} is estimated to be $1.8 \times 10^9 \text{ s}^{-1}$, which is about two
 641 orders of magnitude greater than the pseudo-first-order rate constant k'_{R+O_2} (3.0×10^7
 642 s^{-1}). The result reveals that the unimolecular decomposition of S46 is more
 643 competitive than the bimolecular reaction with O₂. The formed OH radicals can once
 644 again participate in the oxidations of styrene and its multifunctional products,
 645 continuing these processes until they are completely consumed.



646
 647 **Figure 6.** PES for the subsequent reactions of P_{S6-add3} in the presence of O₂ at the
 648 M06-2X/6-311++G(3df,3pd)//M06-2X/6-31+g(d,p) level

649 **3.3.2 The oxidation mechanism of 2nd-RONO₂ initiated by OH**
 650 **radicals**

651 OH-initiated oxidation of 2nd-RONO₂ (S26) includes four different OH-addition
652 pathways and five different H-abstraction pathways, as displayed in Figures S19 and
653 S20. For the OH-addition reactions, the attack of OH radicals on the C3-site of the
654 C₃=C₄ double bond forming the product P_{S26-add3}, occurring on the same direction
655 relative to the -ONO₂ group, is found to be the favorable pathway ($\Delta E_a = 2.4$
656 kcal/mol, $\Delta E_r = -33.6$ kcal/mol). For the H-abstraction reactions, the abstraction of
657 hydrogen atom at the C5-site is identified as the preferable pathway ($\Delta E_a = 5.7$
658 kcal/mol, $\Delta E_r = -20.1$ kcal/mol) due to the enhanced stability of the resulting product
659 P_{S26-add5} by the presence of an allyl group. By comparing the values of ΔE_a and ΔE_r of
660 the favorable OH-addition and H-abstraction pathways, it can be concluded that the
661 former case is dominant on both thermochemically and kinetically. This conclusion is
662 consistent with the result from the reaction 2nd-ROOH (S6) + OH that OH-addition is
663 more competitive than H-abstraction.

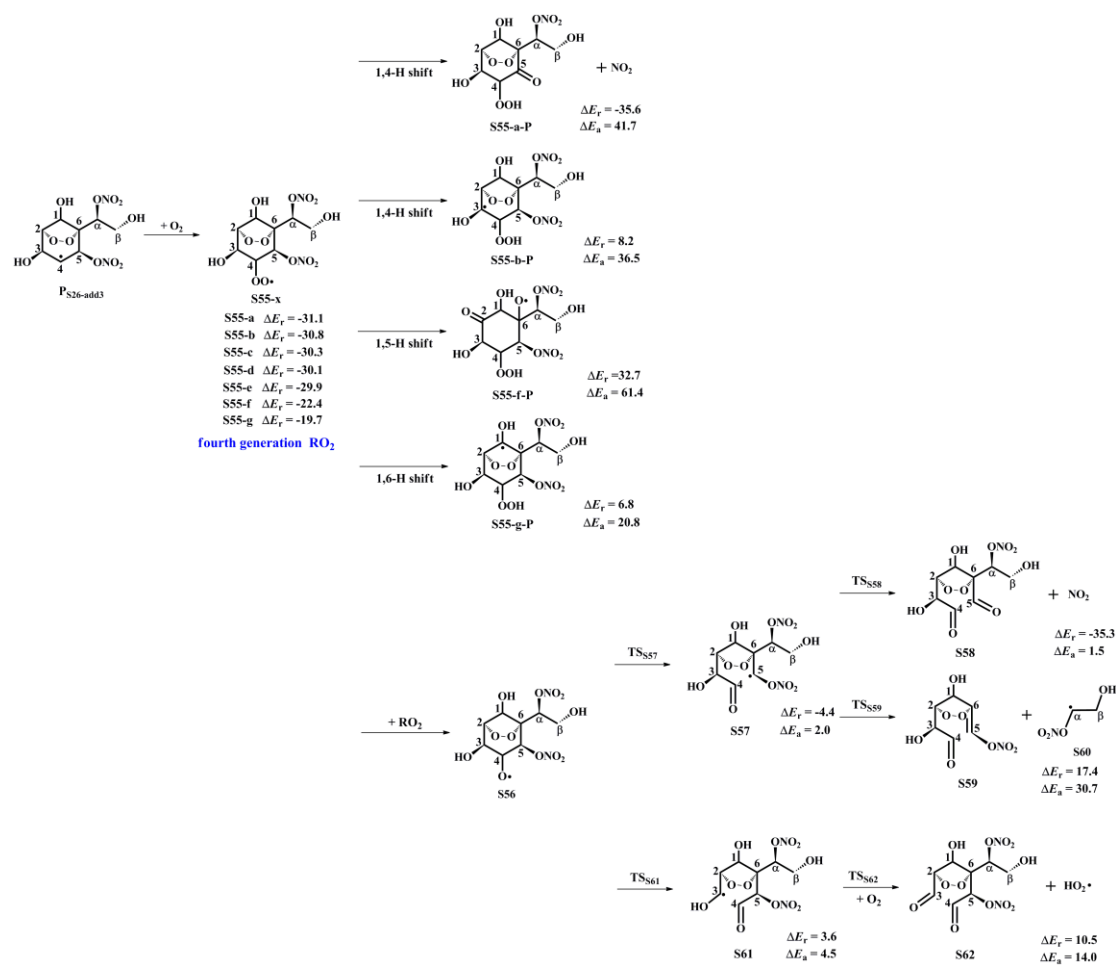
664 The product P_{S26-add3} arising from the favorable OH-addition pathway has three
665 potential unimolecular decay pathways, as depicted in Figure S21: (1) P_{S26-add3}
666 dissociates to an epoxide S52 and a NO₂ molecule through a cyclization process with
667 the ΔE_a of 18.5 kcal/mol and the rate coefficient k_{R52} of 0.4 s⁻¹; (2) P_{S26-add3} isomerizes
668 to an alkyl radical S53 via the intramolecular 1,2 H-shift ($\Delta E_a = 40.0$ kcal/mol); (3)
669 P_{S26-add3} converts into an alkene S54 via the elimination of hydrogen atom ($\Delta E_a = 39.1$
670 kcal/mol). Based on the value of ΔE_a and the corresponding rate coefficient, the
671 dominant pathway of the unimolecular decomposition of P_{S26-add3} is the formation of
672 S52. k_{R52} is about seven orders of magnitude lower than the pseudo-first-order rate
673 constant k'_{R+O_2} , indicating that the unimolecular decomposition of P_{S26-add3} is less
674 importance.

675 In the presence of O₂, P_{S26-add3} can react with an O₂ molecule leading to the
676 formation of the fourth generation peroxy radicals S55-x, comprising seven possible
677 conformers as shown in Figure 7. For the intramolecular H-shifts of S55-x, not all of
678 reactants (S55-c, S55-d and S55-e) have the suitable conformers that allow for the
679 pathways across the reaction barriers. The barriers of intramolecular H-shifts are
680 considerably high ($\Delta E_a = 20.8$ kcal/mol), making them uncompetitive in the

681 atmosphere. Alternatively, S55-x can react with other RO₂ radicals forming an alkoxy
682 radical S56, followed by decomposition into an alkyl radical S57 via the breakage of
683 C₄-C₅ bond ($\Delta E_a = 2.0$ kcal/mol), or fragmentation into an alkyl radical S61 through
684 the cleavage of C₃-C₄ bond ($\Delta E_a = 4.5$ kcal/mol). The aforementioned results reveal
685 that the formation of S57 is energetically favorable, which is consistent with the
686 conclusion derived from the unimolecular decomposition of S45 that the breakage of
687 C₄-C₅ bond is feasible. Next, S57 dissociates to a NO₂ coproduct and a C₈-product
688 S58 that possessed a -NO₃, a peroxide bridge, two carbonyls, and three hydroxy
689 groups. This pathway is expected to be the dominant one ($\Delta E_a = 1.5$ kcal/mol), with
690 the rate coefficient k_{RS58} of 1.2×10^9 s⁻¹. The resulting NO₂ can further participate in
691 the cycling of NO_x, ultimately generating tropospheric ozone and SOA.

692 The overall reaction mechanism and the fractional yields of the major products in
693 the multi-generation OH oxidation of styrene under different NO_x conditions are
694 presented in Figures S22 and S23. In the low-NO_x conditions, the fractional yield of
695 the first generation closed-shell product 1st-ROOH (S4) formed from the reaction
696 S2-1-x + HO₂ · is predicted to be 71.6%. For the second generation OH oxidation, the
697 reaction of the peroxy radical P_{S4-add3-a-2} with HO₂ radicals produces the second
698 generation closed-shell product 2nd-ROOH (S6) and an alkoxy radical P_{S4-add3-a-3},
699 with the fractional yields of 41.4% and 10.4%, respectively. The formed P_{S4-add3-a-2}
700 can either proceed through the C₅-C₆ bond scission to produce an alkyl radical S7 with
701 the fractional yield of 7.8%, or undergo via a cyclization process to generate an alkyl
702 radical S15 with the fractional yield of 2.6%. S7 and S15 can be transformed via a
703 series of reactions, ultimately leading to the formation of second generation
704 closed-shell product S10-2, S13 and S23, with the fractional yields of 5.6%, 2.2% and
705 1.3%, respectively. For the third generation OH oxidation, the degradation of
706 2nd-ROOH (S6) ultimately yields the third generation closed-shell products S47 and
707 S51, with the fractional yields of 26.3% and 0.3%, respectively. As a result, the major
708 closed-shell products are 1st-ROOH (S4), 2nd-ROOH (S6), S10-2, S13 and S47 in the
709 multi-generation OH oxidation of styrene in the low-NO_x conditions.

710 In the high-NO_x conditions, the fractional yield of the first generation
711 closed-shell product 1st-RONO₂ (S5) formed from the reaction S2-1-x + NO is
712 predicted to be 26.5%, as shown in Figure S23. As the OH oxidation reactions
713 proceed, 1st-RONO₂ (S5) can be initially transformed into the peroxy radical
714 P_{S5-add3-a-2}, followed by reaction with NO to form the second generation closed-shell
715 product 2nd-RONO₂ (S26) and an alkoxy radical P_{S5-add3-a-3}, with the fractional
716 yields of 4.8% and 11.2%, respectively. The decomposition of P_{S5-add3-a-3} undergoes
717 via two distinct pathways. One is the C₅-C₆ bond cleavage, leading to an alkyl radical
718 S27 with the fractional yield of 7.8%. The other is the cyclization, resulting in an
719 alkyl radical S35 with the fractional yield of 3.4%. The resulting S27 and S35
720 undergo multiple oxidation steps, finally leading to the formation of the second
721 generation closed-shell products S30-2, S33 and S40-1, with the fractional yields of
722 6.0%, 1.8%, and 1.7%, respectively. 2nd-RONO₂ (S26) can be further oxidized to
723 yield the third generation closed-shell products S58 and S62, with the fractional yields
724 of 2.6% and 0.03%, respectively. In summary, the major closed-shell products are
725 1st-RONO₂ (S5), 2nd-RONO₂ (S26), S30-2 and S58 in the multi-generation OH
726 oxidation of styrene in the high-NO_x conditions.



727

728 **Figure 7.** PES for the subsequent reactions of $\text{P}_{\text{S26-add3}}$ in the presence of O_2 at the
 729 M06-2X/6-311++G(3df,3pd)//M06-2X/6-31+g(d,p) level

730 3.4 Volatility classes

731 The volatility classes for various organic compounds are based on their
 732 saturation concentration, as proposed by Donahue et al. (2012). The saturated vapour
 733 pressure (P^0) and saturated concentration (c^0) of styrene and its multi-generation OH
 734 oxidation products are predicted by using the SIMPOL.1 method (Pankow et al.,
 735 2008). As show in Table S8, the P^0 and c^0 of the first generation closed-shell product
 736 benzaldehyde ($\text{C}_7\text{H}_6\text{O}$) are 7.62×10^{-4} atm and 2.89×10^6 ug/m³, respectively, which
 737 are 3-4 orders of magnitude greater than those of S4 ($\text{C}_8\text{H}_{10}\text{O}_3$, $P^0 = 1.43 \times 10^{-7}$ atm
 738 and $c^0 = 8.89 \times 10^2$ ug/m³) and S5 ($\text{C}_8\text{H}_9\text{NO}_3$, $P^0 = 2.54 \times 10^{-7}$ atm and $c^0 = 1.87 \times$
 739 10^3 ug/m³). Based on the values of c^0 , benzaldehyde is classified as the volatile
 740 organic compounds (VOCs), whereas S4 and S5 are classified as the intermediate
 741 volatility organic compounds (IVOCs). These first generation closed-shell products
 742 exist exclusively in the gas phase under atmospheric conditions (Bianchi et al., 2019).

743 For the second generation closed-shell products, S6 ($C_8H_{12}O_8$, $c^0 = 4.50 \times 10^{-2}$
744 ug/m^3) and S26 ($C_8H_{10}N_2O_{10}$, $c^0 = 0.18 ug/m^3$) formed from the bimolecular reactions
745 with HO_2 radicals and NO are classified as the low volatility organic compounds
746 (LVOCs). Similarly, S13 ($C_8H_{10}O_8$, $c^0 = 2.97 \times 10^{-2} ug/m^3$) and S33 ($C_8H_{10}O_8$, $c^0 =$
747 $2.97 \times 10^{-2} ug/m^3$), formed through the ring-opening and subsequent intramolecular
748 H-shift reactions of $P_{S4-add3-a-3}$ and $P_{S5-add3-a-3}$, respectively, are also classified as
749 LVOCs, which can condense onto the existing large particles (Bianchi et al., 2019).
750 The c^0 values of the remaining closed-shell products are significantly greater than
751 those of the aforementioned four products, for example, the c^0 values of S20 ($C_6H_8O_6$)
752 and S40-1 ($C_6H_7NO_7$), formed by the cyclization and decomposition reactions of
753 $P_{S4-add3-a-3}$ and $P_{S5-add3-a-3}$, are 42.21 and 75.86 ug/m^3 , respectively, classifying them
754 as the semivolatile organic compounds (SVOC).

755 For the third generation closed-shell products, the c^0 values of S47 ($C_8H_{12}O_9$, c^0
756 $= 2.68 \times 10^{-4} ug/m^3$) and S51 ($C_8H_{10}O_{10}$, $c^0 = 1.58 \times 10^{-4} ug/m^3$), formed through the
757 O_2 -addition and subsequent decomposition reactions of $P_{S6-add3}$, are about two orders
758 of magnitude lower than those of the second generation closed-shell products S6 and
759 S13, despite being classified as LVOCs. Similarly, S58 ($C_8H_{11}NO_{10}$, $c^0 = 5.37 \times 10^{-4}$
760 ug/m^3) and S62 ($C_8H_{10}N_2O_{12}$, $c^0 = 6.18 \times 10^{-4} ug/m^3$), formed via the O_2 -addition and
761 subsequent decomposition reactions of $P_{S26-add3}$, exhibit lower c^0 values compared to
762 the second generation closed-shell products S26 and S33. The aforementioned results
763 reveal that the volatility of the multi-generation OH oxidation products significantly
764 decreases with increasing the number of OH oxidation steps. As the oxidation
765 reactions of the third generation closed-shell products proceed further, the formed
766 products may possess sufficiently low volatility to participate in the formation and
767 growth of new aerosol particle.

768 **4 Conclusions and atmospheric implications**

769 The results reveal that the first generation RO_2 radicals, formed from the
770 addition of OH radicals to the C_β -site of a vinyl group in styrene followed by
771 O_2 -addition, can proceed intramolecular H-shifts to generate various alkyl and alkoxy

772 radicals. The rate coefficient $k_{\text{MC-TST}}$ is calculated to be $1.6 \times 10^{-4} \text{ s}^{-1}$. Among the
773 competing H-shift pathways, the hydrogen atom transfer from the $-\text{OH}$ group to the
774 terminal oxygen atom of the $-\text{OO}$ group has the lowest barrier. The resulting alkoxy
775 radical can further decompose into benzaldehyde through the successive elimination
776 of HCHO and an OH radical. The 1,5-H shift reaction occurring at the $-\text{OH}$ group is
777 the rate-determining step in the formation of benzaldehyde. Alternatively, the first
778 generation RO_2 radicals can proceed bimolecular reactions with HO_2 radicals and NO,
779 leading to the formation of the first generation closed-shell C7- and C8-products
780 $1^{\text{st}}\text{-ROOH}$ ($\text{C}_8\text{H}_{10}\text{O}_3$), benzaldehyde ($\text{C}_7\text{H}_6\text{O}$), and $1^{\text{st}}\text{-RONO}_2$ ($\text{C}_8\text{H}_9\text{NO}_3$).

781 For the second generation OH oxidation, OH-addition reaction occurring at the
782 *ortho*-site of $1^{\text{st}}\text{-ROOH}$ and $1^{\text{st}}\text{-RONO}_2$ has a significant dominance. This is consistent
783 with the analogous reaction systems, toluene + OH and phenol + OH, in which
784 *ortho*-OH-addition reaction is energetically favorable (Wu et al., 2020; Xu and Wang,
785 2013). The resulting alkyl radicals may undergo two O_2 -addition steps and a
786 cyclization process to form BPR, which can react with HO_2 radicals and NO to yield
787 the corresponding BAR, and the second generation closed-shell C8-product
788 $2^{\text{nd}}\text{-ROOH}$ ($\text{C}_8\text{H}_{12}\text{O}_8$) and $2^{\text{nd}}\text{-RONO}_2$ ($\text{C}_8\text{H}_{10}\text{N}_2\text{O}_{10}$), with the fractional yields of 41.4%
789 and 4.8%. The unimolecular decomposition of BAR formed in the reaction $1^{\text{st}}\text{-ROOH}$
790 + OH includes two distinct pathways: (1) ring-opening and followed by
791 decomposition, yielding the multifunctional products S10-2 ($\text{C}_4\text{H}_6\text{O}_5$) and S13
792 ($\text{C}_8\text{H}_{10}\text{O}_8$) with the fractional yields of 5.6% and 2.2%, respectively; or (2) cyclization
793 and followed by dissociation, generating the closed-shell C6-product S23 ($\text{C}_6\text{H}_6\text{O}_5$)
794 with the fractional yield of 1.3%. The major products formed from the unimolecular
795 decomposition of BAR in the reaction $1^{\text{st}}\text{-RONO}_2$ + OH are the multifunctional
796 products S30-2 ($\text{C}_4\text{H}_5\text{NO}_6$), S33 ($\text{C}_8\text{H}_{10}\text{O}_8$) and S40-1 ($\text{C}_6\text{H}_7\text{NO}_7$), with the fractional
797 yields of 6.0%, 1.8% and 1.7%, respectively.

798 For the third generation OH oxidation, the addition of OH radicals to the C=C
799 bond in $2^{\text{nd}}\text{-ROOH}$ and $2^{\text{nd}}\text{-RONO}_2$ is the dominant pathway. The resulting alkyl
800 radicals can proceed a series of reactions to produce the alkoxy radicals, which
801 subsequently decompose into an OH radical byproduct and a closed-shell C₈-product

802 S47 ($C_8H_{12}O_9$), identified as the favorable pathway in the reaction 2^{nd} -ROOH + OH.
803 S47 contains a –OOH, a peroxide bridge, two carbonyls, and three hydroxy groups.
804 The major product formed in the reaction 2^{nd} -RONO₂ + OH is a closed-shell
805 C₈-product S58 ($C_8H_{11}NO_{10}$), which contain a –NO₃, a peroxide bridge, two carbonyls,
806 and three hydroxy groups. The fractional yields of S47 and S58 are 26.3% and 2.6%,
807 respectively. The volatility of the oxidation products significantly decreases with
808 increasing the number of OH oxidation steps in the multi-generation OH oxidation
809 of styrene.

810 In the laboratory chamber experiments, the structures of some specific oxidation
811 products remain uncharacterized but are merely inferred from the exact mass and
812 fragmentation data. Using high-level quantum chemistry methods, we identify the
813 molecular structures of multifunctional products and elucidate their formation
814 pathways in the multi-generation OH oxidation of styrene. The mechanistic insights
815 derived from this work are broadly applicable to the photooxidation of structurally
816 analogous aromatics. Furthermore, we quantify the yields of multifunctional products
817 and demonstrate that their volatility decreases significantly with increasing the
818 number of OH oxidation steps. The resulting multifunctional products may undergo a
819 series of oxidation reactions to form low volatility compounds, thereby contributing to
820 the formation and growth of new aerosol particle. In the future, more detailed
821 experimental and theoretical studies need to be conducted to identify the molecular
822 structures and formation pathways of multifunctional products formed through the
823 photooxidation of other aromatics under both low and high-NO_x conditions. These
824 studies will facilitate a more accurate characterization of the chemical composition
825 and formation yields of aromatic SOA, and thereby help narrow the gap between the
826 measured and modeled SOA concentrations in urban environments.

827

828 **Data availability**

829 Datasets are accessible by contacting the corresponding author, Yu Huang,
830 (huangyu@ieecas.cn).

831

832 **Supplement**

833 Tables S1 and S3 list the energy barriers of all the elementary reactions involved
834 in the addition of OH radicals to styrene and 1st-ROOH (S4) predicted at different
835 levels. Tables S2, S4 and S6 list the relative electronic energy, free energy and
836 Boltzmann population of different conformers involved in S2-1-x, S8-x and S28-x.
837 Tables S5 and S7 list the MC-TST rate coefficients for the intramolecular H-shift
838 reactions of S8-x and S28-x. Table S8 summaries the saturated vapour pressure and
839 saturated concentrations of styrene and its multiple generation OH oxidation
840 closed-shell products. Figures S1-S3 display the PESs for the unimolecular reactions
841 of S2-2-x, S2-3-x and S2-4-x. Figure S4 shows the global minimum structures of
842 1st-ROOH(S4) and 1st-RONO₂(S5). Figure S5 depicts the geometric parameters of
843 toluene and 1st-ROOH (S4) and the NPA atomic charges of all the carbon atoms.
844 Figures S6 and S11 show the PESs for the addition reactions P_{S4-add1} + O₂ and P_{S5-add1}
845 + O₂. Figures S7 and S12 present the lowest energy conformers of third generation
846 peroxy radicals P_{S4-add3-a-2} and P_{S5-add3-a-2}. Figures S8-S10 depict the PESs for the
847 intramolecular hydrogen transfer reactions of S8-x, S12-x and S16-x. Figures
848 S13-S15 depict the PESs for the intramolecular hydrogen transfer reactions of S28-x,
849 S32-x and S36-x. Figures S16-18 show the PESs for the OH-initiated oxidation of
850 2nd-ROOH (S6) and unimolecular decomposition of P_{S6-add3}. Figures S19-S21 show
851 the PESs for the OH-initiated oxidation of 2nd-RONO₂ (S26) and unimolecular
852 decomposition of P_{S26-add3}. Figures S22 and S23 show the overall reaction mechanism
853 of the multi-generation OH oxidation of styrene in the low- and high-NO_x conditions.

854

855 **Author contribution**

856 LC and YH conceptualized the study. LC conducted quantum chemical
857 calculation. YX and ZJ analyzed the data. LC conducted the volatility estimation. All
858 authors discussed the results and commented on the manuscript.

859

860 **Competing interests**

861 The contact author has declared that none of the authors has any competing
862 interests.

863

864 **Financial support**

865 This study was supported by the National Natural Science Foundation of China
866 (grant nos. 42175134) and the Youth Innovation Promotion Association of the
867 Chinese Academy of Sciences (grant number 2022415).

868

869 **Reference**

- 870 Alecu, I. M., Zheng, J., Zhao, Y., and Truhlar, D. G.: Computational thermochemistry: scale factor
871 databases and scale factors for vibrational frequencies obtained from electronic model
872 chemistries, *J. Chem. Theory Comput.*, 6, 2872-2887, <https://doi.org/10.1021/ct100326h>,
873 2010.
- 874 Arathala, P., and Musah, R. A.: Atmospheric chemistry of chloroprene initiated by OH radicals:
875 combined Ab initio/DFT calculations and kinetics analysis, *J. Phys. Chem. A*, 128,
876 8983-8995, <https://doi.org/10.1021/acs.jpca.4c05428>, 2024.
- 877 Atkinson, R., and Arey, J.: Atmospheric degradation of volatile organic compounds, *Chem. Rev.*,
878 103, 4605-4638, <https://doi.org/10.1021/cr0206420>, 2003.
- 879 Bianchi, F., Kurt n, T., Riva, M., Mohr, C., Rissanen, M. P., Roldin, P., Berndt, T., Crouse, J. D.,
880 Wennberg, P. O., Mentel, T. F., Wildt, J., Junninen, H., Jokinen, T., Kulmala, M., Worsnop, D.
881 R., Thornton, J. A., Donahue, N., Kjaergaard, H. G., and Ehn, M.: Highly oxygenated organic
882 molecules (HOM) from gas-phase autoxidation involving peroxy radicals: a key contributor
883 to atmospheric aerosol, *Chem. Rev.*, 119, 3472-3509,
884 <https://doi.org/10.1021/acs.chemrev.8b00395>, 2019.
- 885 Bloss, C., Wagner, V., Jenkin, M. E., Volkamer, R., Bloss, W. J., Lee, J. D., Heard, D. E., Wirtz, K.,
886 Martin-Reviejo, M., Rea, G., Wenger, J. C., and Pilling, M. J.: Development of a detailed
887 chemical mechanism (MCMv3.1) for the atmospheric oxidation of aromatic hydrocarbons,
888 *Atmos. Chem. Phys.*, 5, 641-664, <https://doi.org/10.5194/acp-5-641-2005>, 2005.
- 889 Boyd, A. A., Flaud, P. M., Daugey, N., and Lesclaux, R.: Rate constants for RO₂ + HO₂ reactions
890 measured under a large excess of HO₂, *J. Phys. Chem. A*, 107, 818-821,
891 <https://doi.org/10.1021/jp026581r>, 2003.
- 892 Cabrera-Perez, D., Taraborrelli, D., Sander, R., and Pozzer, A.: Global atmospheric budget of
893 simple monocyclic aromatic compounds, *Atmos. Chem. Phys.*, 16, 6931-6947,
894 <https://doi.org/10.5194/acp-16-6931-2016>, 2016.
- 895 Canneaux, S., Bohr, F., and Henon, E.: KiSThelP: a program to predict thermodynamic properties
896 and rate constants from quantum chemistry results, *J. Comput. Chem.*, 35, 82-93,
897 <https://doi.org/10.1002/jcc.23470>, 2013.

898 Chen, L., Huang, Y., Xue, Y., Jia, Z., and Wang, W.: Atmospheric oxidation of 1-butene initiated
899 by OH radical: Implications for ozone and nitrous acid formations, *Atmos. Environ.*, 244,
900 118010-118021, <https://doi.org/10.1016/j.atmosenv.2020.118010>, 2021.

901 Cho, J., Roueintan, M., and Li, Z.: Kinetic and dynamic investigations of OH reaction with
902 styrene, *J. Phys. Chem. A*, 118, 9460-9470, <https://doi.org/10.1021/jp501380j>, 2014.

903 Donahue, N. M., Kroll, J. H., Pandis, S. N., and Robinson, A. L.: A two-dimensional volatility
904 basis set – Part 2: Diagnostics of organic-aerosol evolution, *Atmos. Chem. Phys.*, 12,
905 615-634, <https://doi.org/10.5194/acp-12-615-2012>, 2012.

906 Eckart, C.: The penetration of a potential barrier by electrons, *Phys. Rev.*, 35, 1303-1309,
907 <https://doi.org/10.1103/PhysRev.35.1303>, 1930.

908 Environmental Protection Agency (EPA). Clean Air Act: Title I-Air Pollution Prevention and
909 Control. U.S. 1990.

910 Fernández-Ramos, A., Ellingson, B. A., Meana-Pañeda, R., Marques, J. M. C., and Truhlar, D. G.:
911 Symmetry numbers and chemical reaction rates, *Theor. Chem. Acc.*, 118, 813-826,
912 <https://doi.org/10.1007/s00214-007-0328-0>, 2007.

913 Forstner, H. J. L., Flagan, R. C., and Seinfeld, J. H.: Secondary organic aerosol from the
914 photooxidation of aromatic hydrocarbons: molecular composition, *Environ. Sci. Technol.*, 31,
915 1345-1358, <https://doi.org/10.1021/es9605376>, 1997.

916 Frisch, M. J., Trucks, G. W., Schlegel, H. B., Scuseria, G. E., Robb, M. A., Cheeseman, J. R.,
917 Scalmani, G., Barone, V., Petersson, G. A., Nakatsuji, H., Li, X., Caricato, M., Marenich, A.
918 V., Bloino, J., Janesko, B. G., Gomperts, R., Mennucci, B., Hratchian, H. P., Ortiz, J. V.,
919 Izmaylov, A. F., Sonnenberg, J. L., Williams-Young, D., Ding, F., Lipparini, F., Egidi, F.,
920 Goings, J., Peng, B., Petrone, A., Henderson, T., Ranasinghe, D., Zakrzewski, V. G., Gao, J.,
921 Rega, N., Zheng, G., Liang, W., Hada, M., Ehara, M., Toyota, K., Fukuda, R., Hasegawa, J.,
922 Ishida, M., Nakajima, T., Honda, Y., Kitao, O., Nakai, H., Vreven, T., Throssell, K.,
923 Montgomery, J. A., Peralta, J. J. E., Ogliaro, F., Bearpark, M. J., Heyd, J. J., Brothers, E. N.,
924 Kudin, K. N., Staroverov, V. N., Keith, T. A., Kobayashi, R., Normand, J., Raghavachari, K.,
925 Rendell, A. P., Burant, J. C., Iyengar, S. S., Tomasi, J., Cossi, M., Millam, J. M., Klene, M.,
926 Adamo, C., Cammi, R., Ochterski, J. W., Martin, R. L., Morokuma, K., Farkas, O., Foresman,
927 J. B., and Fox, D. J.: Gaussian 16, Revision B.01, Gaussian, Inc., Wallingford CT, 2016.

928 Fu, Z., Guo, S., Xie, H. B., Zhou, P., Boy, M., Yao, M., and Hu, M.: A near-explicit reaction
929 mechanism of chlorine-initiated limonene: implications for health risks associated with the
930 concurrent use of cleaning agents and disinfectants, *Environ. Sci. Technol.*, 58, 19762-19773,
931 <https://doi.org/10.1021/acs.est.4c04388>, 2024.

932 Fu, Z., Ma, F., Liu, Y., Yan, C., Huang, D., Chen, J., Elm, J., Li, Y., Ding, A., Pichelstorfer, L., Xie,
933 H. B., Nie, W., Francisco, J. S., and Zhou, P.: An overlooked oxidation mechanism of toluene:
934 computational predictions and experimental validations, *Chem. Sci.*, 14, 13050-13059,
935 <https://doi.org/10.1039/D3SC03638C>, 2023.

936 Fu, Z., Xie, H. B., Elm, J., Guo, X., Fu, Z., and Chen, J.: Formation of low-volatile products and
937 unexpected high formaldehyde yield from the atmospheric oxidation of methylsiloxanes,
938 *Environ. Sci. Technol.*, 54, 7136-7145, <https://doi.org/10.1021/acs.est.0c01090>, 2020.

939 Fukui, K.: The path of chemical reactions - the IRC approach, *Acc. Chem. Res.*, 14, 363-368,
940 <https://doi.org/10.1021/ar00072a001>, 1981.

941 Garmash, O., Rissanen, M. P., Pullinen, I., Schmitt, S., Kausiala, O., Tillmann, R., Zhao, D.,

942 Percival, C., Bannan, T. J., Priestley, M., Hallquist, Å M., Kleist, E., Kiendler-Scharr, A.,
943 Hallquist, M., Berndt, T., McFiggans, G., Wildt, J., Mentel, T. F., and Ehn, M.:
944 Multi-generation OH oxidation as a source for highly oxygenated organic molecules from
945 aromatics, *Atmos. Chem. Phys.*, 20, 515-537, <https://doi.org/10.5194/acp-20-515-2020>, 2020.

946 Gilbert, R. G., and Smith, S. C.: *Theory of unimolecular and recombination reactions*, Blackwell
947 Scientific: Carlton, Australia, 1990.

948 Glowacki, D. R., Liang, C. H., Morley, C., Pilling, M. J., and Robertson, S. H.: MESMER: an
949 open-source master equation solver for multi-energy well reactions, *J. Phys. Chem. A*, 116,
950 9545-9560, <https://doi.org/10.1021/jp3051033>, 2012.

951 Holbrook, K. A., Pilling, M. J., Robertson, S. H., and Robinson, P. J.: *Unimolecular reactions*, 2nd
952 ed.; Wiley: New York, 1996.

953 Huang, Y., Su, T., Wang, L., Wang, N., Xue, Y., Dai, W., Lee, S. C., Cao, J., and Ho, S. S. H.:
954 Evaluation and characterization of volatile air toxics indoors in a heavy polluted city of
955 northwestern China in wintertime, *Sci. Total Environ.*, 662, 470-480,
956 <https://doi.org/10.1016/j.scitotenv.2019.01.250>, 2019.

957 Iuga, C., Galano, A., and Vivier-Bunge, A.: Theoretical investigation of the OH-initiated oxidation
958 of benzaldehyde in the troposphere, *Chem. Phys. Chem.*, 9, 1453-1459,
959 <https://doi.org/10.1002/cphc.200800144>, 2008.

960 Iyer, S., Kumar, A., Savolainen, A., Barua, S., Daub, C., Pichelstorfer, L., Roldin, P., Garmash, O.,
961 Seal, P., Kurt n, T., and Rissanen, M.: Molecular rearrangement of bicyclic peroxy radicals is
962 a key route to aerosol from aromatics, *Nat. Commun.*, 14, 4984-4991,
963 <https://doi.org/10.1038/s41467-023-40675-2>, 2023.

964 Ji, Y., Zhao, J., Terazono, H., Misawa, K., Levitt, N. P., Li, Y., Lin, Y., Peng, J., Wang, Y., Duan, L.,
965 Pan, B., Zhang, F., Feng, X., An, T., Marrero-Ortiz, W., Secret, J., Zhang, A. L., Shibuya, K.,
966 Molina, M. J., and Zhang, R.: Reassessing the atmospheric oxidation mechanism of toluene,
967 *Proc. Natl. Acad. Sci. U.S.A.*, 114, 8169-8174, <https://doi.org/10.1073/pnas.1705463114>,
968 2017.

969 Koppmann, R.: *Volatile organic compounds in the atmosphere*, John Wiley & Sons, 2008.

970 Li, M., Zhang, Q., Zheng, B., Tong, D., Lei, Y., Liu, F., Hong, C., Kang, S., Yan, L., Zhang, Y., Bo,
971 Y., Su, H., Cheng, Y., and He, K.: Persistent growth of anthropogenic non-methane volatile
972 organic compound (NMVOC) emissions in China during 1990-2017: drivers, speciation and
973 ozone formation potential, *Atmos. Chem. Phys.*, 19, 8897-8913,
974 <https://doi.org/10.5194/acp-19-8897-2019>, 2019.

975 Lu, T.: Molclus program, Version 1.9.3. <http://www.keinsci.com/research/molclus.html> (accessed
976 May 21, 2024).

977 Ma, F., Guo, X., Xia, D., Xie, H. B., Wang, Y., Elm, J., Chen, J., and Niu, J.: Atmospheric
978 chemistry of allylic radicals from isoprene: a successive cyclization-driven autoxidation
979 mechanism, *Environ. Sci. Technol.*, 55, 4399-4409, <https://doi.org/10.1021/acs.est.0c07925>,
980 2021.

981 M ller, K. H., Berndt, T., and Kjaergaard, H. G.: Atmospheric autoxidation of amines, *Environ.*
982 *Sci. Technol.*, 54, 11087-11099, <https://doi.org/10.1021/acs.est.0c03937>, 2020.

983 M ller, K. H., Otkjær, R. V., Hyttinen, N., Kurt n, T., and Kjaergaard, H. G.: Cost-effective
984 implementation of multiconformer transition state theory for peroxy radical hydrogen shift
985 reactions, *J. Phys. Chem. A*, 120, 10072-10087, <https://doi.org/10.1021/acs.jpca.6b09370>,

986 2016.

987 Molteni, U., Bianchi, F., Klein, F., Haddad, I. E., Frege, C., Rossi, M. J., Dommen, J., and
988 Baltensperger, U.: Formation of highly oxygenated organic molecules from aromatic
989 compounds, *Atmos. Chem. Phys.*, 18, 1909-1921, <https://doi.org/10.5194/acp-18-1909-2018>,
990 2018.

991 Neese, F.: Software update: the ORCA program system—version 6.0, *Wires Comput. Mol. Sci.*, 15,
992 e70019, <https://doi.org/10.1002/wcms.70019>, 2025.

993 Nie, W., Yan, C., Huang, D. D., Wang, Z., Liu, Y., Qiao, X., Guo, Y., Tian, L., Zheng, P., Xu, Z., Li,
994 Y., Xu, Z., Qi, X., Sun, P., Wang, J., Zheng, F., Li, X., Yin, R., Dallenbach, K. R., Bianchi, F.,
995 Petřá T., Zhang, Y., Wang, M., Schervish, M., Wang, S., Qiao, L., Wang, Q., Zhou, M.,
996 Wang, H., Yu, C., Yao, D., Guo, H., Ye, P., Lee, S., Li, Y. J., Liu, Y., Chi, X., Kerminen, V. M.,
997 Ehn, M., Donahue, N. M., Wang, T., Huang, C., Kulmala, M., Worsnop, D., Jiang, J., and
998 Ding, A.: Secondary organic aerosol formed by condensing anthropogenic vapours over
999 China's megacities, *Nat. Geosci.*, 15, 255-261, <https://doi.org/10.1038/s41561-022-00922-5>,
1000 2022.

1001 Orlando, J. J., and Tyndall, G. S.: Laboratory studies of organic peroxy radical chemistry: an
1002 overview with emphasis on recent issues of atmospheric significance, *Chem. Soc. Rev.*, 41,
1003 6294-6317, <https://doi.org/10.1039/C2CS35166H>, 2012.

1004 Pankow, J. F., and Asher, W. E.: SIMPOL.1: a simple group contribution method for predicting
1005 vapor pressures and enthalpies of vaporization of multifunctional organic compounds, *Atmos.*
1006 *Chem. Phys.*, 8, 2773-2796, <https://doi.org/10.5194/acp-8-2773-2008>, 2008.

1007 Pasik, D., Frandsen, B. N., Meder, M., Iyer, S., Kurtén, T., and Myllys, N.: Gas-phase oxidation of
1008 atmospherically relevant unsaturated hydrocarbons by acyl peroxy radicals, *J. Am. Chem.*
1009 *Soc.*, 146, 13427-13437, <https://doi.org/10.1021/jacs.4c02523>, 2024.

1010 Sebbar, N., Bozzelli, J. W., and Bockhorn, H.: Thermochemistry and reaction paths in the
1011 oxidation reaction of benzoyl radical: C₆H₅C(=O), *J. Phys. Chem. A*, 115, 11897-11914,
1012 <https://doi.org/10.1021/jp2078067>, 2011.

1013 Shen, H., Vereecken, L., Kang, S., Pullinen, I., Fuchs, H., Zhao, D., and Mentel, T. F.: Unexpected
1014 significance of a minor reaction pathway in daytime formation of biogenic highly oxygenated
1015 organic compounds, *Sci. Adv.*, 8, eabp8702, <https://doi.org/10.1126/sciadv.abp8702>, 2022.

1016 Sun, J., Wu, F., Hu, B., Tang, G., Zhang, J., and Wang, Y.: VOC characteristics, emissions and
1017 contributions to SOA formation during hazy episodes, *Atmos. Environ.*, 141, 560-570,
1018 <https://doi.org/10.1016/j.atmosenv.2016.06.060>, 2016.

1019 Tajuelo, M., Bravo, I., Rodríguez, A., Aranda, A., Dáz-de-Mera, Y., and Rodríguez, D.:
1020 Atmospheric sink of styrene, α -methylstyrene, trans- β -methylstyrene and indene: Rate
1021 constants and mechanisms of Cl atom-initiated degradation, *Atmos. Environ.*, 200, 78-89,
1022 <https://doi.org/10.1016/j.atmosenv.2018.11.059>, 2019c.

1023 Tajuelo, M., Rodríguez, A., Baeza-Romero, M. T., Aranda, A., Dáz-de-Mera, Y., and Rodríguez,
1024 D.: Secondary organic aerosol formation from α -methylstyrene atmospheric degradation:
1025 Role of NO_x level, relative humidity and inorganic seed aerosol, *Atmos. Res.*, 230,
1026 104631-104640, <https://doi.org/10.1016/j.atmosres.2019.104631>, 2019b.

1027 Tajuelo, M., Rodríguez, D., Baeza-Romero, M. T., Dáz-de-Mera, Y., Aranda, A., and Rodríguez,
1028 A.: Secondary organic aerosol formation from styrene photolysis and photooxidation with
1029 hydroxyl radicals, *Chemosphere*, 231, 276-286,

1030 <https://doi.org/10.1016/j.chemosphere.2019.05.136>, 2019a.

1031 Vereecken, L., Glowacki, D. R., and Pilling, M. J.: Theoretical chemical kinetics in tropospheric
1032 chemistry: methodologies and applications, *Chem. Rev.*, 115, 4063-4114,
1033 <https://doi.org/10.1021/cr500488p>, 2015.

1034 Wang, H., Ji, Y., Gao, Y., Li, G., and An, T.: Theoretical model on the formation possibility of
1035 secondary organic aerosol from OH initiated oxidation reaction of styrene in the presence of
1036 O₂/NO, *Atmos. Environ.*, 101, 1-9, <https://doi.org/10.1016/j.atmosenv.2014.10.042>, 2015.

1037 Wang, L., Wu, R., and Xu, C.: Atmospheric oxidation mechanism of benzene. Fates of alkoxy
1038 radical intermediates and revised mechanism, *J. Phys. Chem. A*, 117, 14163-14168,
1039 <https://doi.org/10.1021/jp4101762>, 2013.

1040 Wang, M., Chen, D., Xiao, M., Ye, Q., Stolzenburg, D., Hofbauer, V., Ye, P., Vogel, A. L., Mauldin,
1041 R. L., Amorim, A., Baccarini, A., Baumgartner, B., Brilke, S., Dada, L., Dias, A., Duplissy, J.,
1042 Finkenzeller, H., Garmash, O., He, X. C., Hoyle, C. R., Kim, C., Kvashnin, A., Lehtipalo, K.,
1043 Fischer, L., Molteni, U., Petřáková, T., Pospisilova, V., Quéléver, L. L. J., Rissanen, M., Simon,
1044 M., Tauber, C., Tomé, A., Wagner, A. C., Weitz, L., Volkamer, R., Winkler, P. M., Kirkby, J.,
1045 Worsnop, D. R., Kulmala, M., Baltensperger, U., Dommen, J., El-Haddad, I., and Donahue,
1046 N. M.: Photo-oxidation of aromatic hydrocarbons produces low-volatility organic compounds,
1047 *Environ. Sci. Technol.*, 54, 7911-7921, <https://doi.org/10.1021/acs.est.0c02100>, 2020.

1048 Wang, S., and Li, H.: NO₃-initiated gas-phase formation of nitrated phenolic compounds in
1049 polluted atmosphere, *Environ. Sci. Technol.*, 55, 2899-2907,
1050 <https://doi.org/10.1021/acs.est.0c08041>, 2021.

1051 Wang, S., Newland, M. J., Deng, W., Rickard, A. R., Hamilton, J. F., Muñoz, A., Ródenas, M.,
1052 Vázquez, M. M., Wang, L., and Wang, X.: Aromatic photo-oxidation, a new source of
1053 atmospheric acidity, *Environ. Sci. Technol.*, 54, 7798-7806,
1054 <https://doi.org/10.1021/acs.est.0c00526>, 2020.

1055 Wang, S., Wu, R., Berndt, T., Ehn, M., and Wang, L.: Formation of highly oxidized radicals and
1056 multifunctional products from the atmospheric oxidation of alkylbenzene, *Environ. Sci.*
1057 *Technol.*, 51, 8442-8449, <https://doi.org/10.1021/acs.est.7b02374>, 2017.

1058 Wu, R., Pan, S., Li, Y., and Wang, L.: Atmospheric oxidation mechanism of toluene, *J. Phys.*
1059 *Chem. A*, 118, 4533-4547, <https://doi.org/10.1021/jp500077f>, 2014.

1060 Wu, X., Hou, Q., Huang, J., Chai, J., and Zhang, F.: Exploring the OH-initiated reactions of
1061 styrene in the atmosphere and the role of van der Waals complex, *Chemosphere*, 282,
1062 131004-131012, <https://doi.org/10.1016/j.chemosphere.2021.131004>, 2021.

1063 Wu, X., Huang, C., Niu, S., and Zhang, F.: New theoretical insights into the reaction kinetics of
1064 toluene and hydroxyl radicals, *Phys. Chem. Chem. Phys.*, 22, 22279-22288,
1065 <https://doi.org/10.1039/D0CP02984J>, 2020.

1066 Xu, C., and Wang, L.: Atmospheric oxidation mechanism of phenol initiated by OH radical, *J.*
1067 *Phys. Chem. A*, 117, 2358-2364, <https://doi.org/10.1021/jp308856b>, 2013.

1068 Xu, L., Møller, K. H., Crouse, J. D., Kjaergaard, H. G., and Wennberg, P. O.: New insights into
1069 the radical chemistry and product distribution in the OH-initiated oxidation of benzene,
1070 *Environ. Sci. Technol.*, 54, 13467-13477, <https://doi.org/10.1021/acs.est.0c04780>, 2020.

1071 Yan, Y., Cabrera-Perez, D., Lin, J., Pozzer, A., Hu, L., Millet, D. B., Porter, W. C., and Lelieveld,
1072 J.: Global tropospheric effects of aromatic chemistry with the SAPRC-11 mechanism
1073 implemented in GEOS-Chem version 9-02, *Geosci. Model Dev.*, 12, 111-130,

1074 <https://doi.org/10.5194/gmd-12-111-2019>, 2019.

1075 Yang, F., Deng, F., Pan, Y., Zhang, Y., Tang, C., and Huang, Z.: Kinetics of hydrogen abstraction
1076 and addition reactions of 3-hexene by OH radicals, *J. Phys. Chem. A*, 121, 1877-1889,
1077 <https://doi.org/10.1021/acs.jpca.6b11499>, 2017.

1078 Yu, S., Jia, L., Xu, Y., and Pan, Y.: Formation of extremely low-volatility organic compounds from
1079 styrene ozonolysis: Implication for nucleation, *Chemosphere*, 305, 135459-135467,
1080 <https://doi.org/10.1016/j.chemosphere.2022.135459>, 2022.

1081 Yu, S., Jia, L., Xu, Y., and Pan, Y.: Molecular composition of secondary organic aerosol from
1082 styrene under different NO_x and humidity conditions, *Atmos. Res.*, 266, 105950-10604,
1083 <https://doi.org/10.1016/j.atmosres.2021.105950>, 2022.

1084 Zaytsev, A., Koss, A. R., Breitenlechner, M., Krechmer, J. E., Nihill, K. J., Lim, C. Y., Rowe, J. C.,
1085 Cox, J. L., Moss, J., Roscioli, J. R., Canagaratna, M. R., Worsnop, D. R., Kroll, J. H., and
1086 Keutsch, F. N.: Mechanistic study of the formation of ring-retaining and ring-opening
1087 products from the oxidation of aromatic compounds under urban atmospheric conditions,
1088 *Atmos. Chem. Phys.*, 19, 15117-15129, <https://doi.org/10.5194/acp-19-15117-2019>, 2019.

1089 Zhang, H., Wang, J., Dong, B., Xu, F., Liu, H., Zhang, Q., Zong, W., and Shi, X.: New mechanism
1090 for the participation of aromatic oxidation products in atmospheric nucleation, *Sci. Total*
1091 *Environ.*, 917, 170487-170494, <https://doi.org/10.1016/j.scitotenv.2024.170487>, 2024.

1092 Zhang, R. M., Truhlar, D. G., and Xu, X.: Kinetics of the toluene reaction with OH radical,
1093 *Research*, 2019, Article ID 5373785, <https://doi.org/10.34133/2019/5373785>, 2019.

1094 Zhao, H., Zhang, Y., Zhao, Q., Li, Y., and Huang, Z.: A theoretical study of H-abstractions of
1095 benzaldehyde by H, O³(P), ³O₂, OH, HO₂, and CH₃ radicals: Ab initio rate coefficients and
1096 their uncertainty quantification, *J. Phys. Chem. A*, 126, 7523-7533,
1097 <https://doi.org/10.1021/acs.jpca.2c02384>, 2022.

1098 Zhao, Y., and Truhlar, D. G.: The M06 suite of density functionals for main group
1099 thermochemistry, thermochemical kinetics, noncovalent interactions, excited states, and
1100 transition elements: two new functionals and systematic testing of four M06-class functionals
1101 and 12 other functionals, *Theor. Chem. Acc.*, 120, 215-241,
1102 <https://doi.org/10.1007/s00214-007-0310-x>, 2008.